Available online at www.sciencedirect.com

ScienceDirect

journal homepage: www.elsevier.com/locate/he

The role of the ceria dopant on Ni / doped-ceria anodic layer cermets for direct ethanol solid oxide fuel cell

A.A.A. da Silva [a,b], M.C. Steil [c], F.N. Tabuti [d], R.C. Rabelo-Neto [e], F.B. Noronha [a,e,f], L.V. Mattos [b], F.C. Fonseca [d,*]

[a] Military Institute of Engineering, Chemical Engineering Department, Praça Gal. Tiburcio 80, Rio de Janeiro, 22290-270, Brazil

[b] Fluminense Federal University, Chemical Engineering Department, Rua Passo da Pátria, 156, Niterói, 24210-240, Brazil

[c] Univ. Grenoble Alpes, Univ. Savoie Mont Blanc, CNRS, Grenoble INP, LEPMI, Grenoble, 38000, France

[d] Instituto de Pesquisas Energéticas Nucleares, IPEN-CNEN/SP, Av. Lineu Prestes 2242, São Paulo, 05508-000, Brazil

[e] National Institute of Technology, Catalysis Division, Av. Venezuela 82, Rio de Janeiro 20081-312, Brazil

[f] Univ. Lille, CNRS, Centrale Lille, ENSCL, Univ. Artois, UMR 8181 — UCCS — Unité de Catalyse et Chimie Du Solide, Lille, F-59000, France

HIGHLIGHTS

- Direct bioethanol solid oxide fuel cells stable for 100 h without water.
- The ceria dopant affects the transport and catalytic properties for ethanol SOFC.
- Ni/doped-ceria catalytic layer ensures ethanol conversion and avoids carbon deposit.

GRAPHICAL ABSTRACT

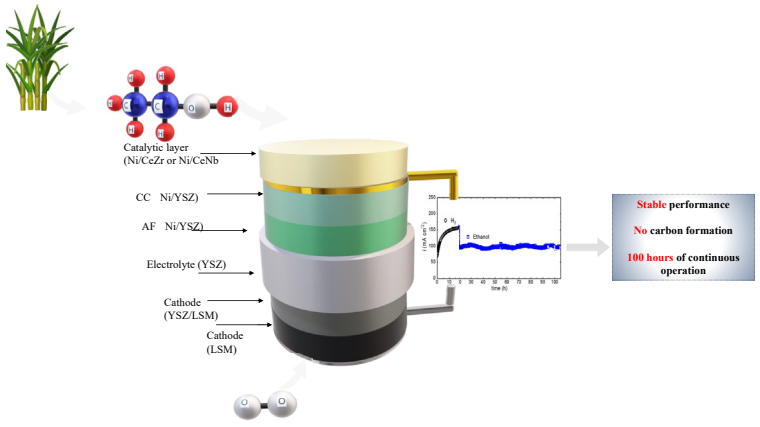

ARTICLE INFO

Article history:
Received 12 August 2020
Received in revised form
17 October 2020

ABSTRACT

The effect of ceria dopant aiming at stability in Ni/doped-ceria anodic layers for direct ethanol solid oxide fuel cells (SOFC) was studied. Solid solutions of ceria doped with Y, Gd, Zr, or Nb (10 mol%) impregnated with NiO were tested in a fixed bed reactor for ethanol conversion reactions and for direct (dry) ethanol SOFC. The ceria dopant showed a marked effect on both the catalytic and the electrical transport properties of the ceramic support.

* *Corresponding author.*
E-mail address: fabiocf@usp.br (F.C. Fonseca).

https://doi.org/10.1016/j.ijhydene.2020.10.155

Accepted 19 October 2020
Available online 9 November 2020

Keywords:
Doped-ceria
Ni/doped-ceria cermet
Ethanol solid oxide fuel cell

Catalytic activity data revealed that the studied materials deactivate in ethanol decomposition reaction but are stable for ethanol steam reforming. Thus, feeding dry ethanol to the SOFC with a Ni/doped-ceria anodic catalytic layer evidenced that water produced from the electrochemical hydrogen oxidation provides steam for the internal reforming resulting in great stability of the fuel cells tested during ~100 h. The combined catalysis and SOFC results demonstrate Ni/doped-ceria is as candidate anode layer for stable SOFC running on bioethanol.

Introduction

Bioethanol is probably the most successful example of a sustainable biofuel. Sugar-cane derived ethanol, differently from ethanol produced from other biomasses, has positive outcomes when energetic and economical parameters are considered. In Brazil, almost 90% of cars can run on ethanol, and a solid industrial infrastructure is responsible for large-scale production and wide distribution across the country. The utilization of such fuel is associated with significant improvement of the air quality in the main metropolitan areas of the country [1]. Such features, along with still inexistent hydrogen infrastructure, have placed ethanol as almost an ideal feedstock for fuel cells. Interest in ethanol is boosted by the e-bio concept electric vehicle by Nissan. Such prototype car uses bioethanol, which is pre-reformed and converted into electricity by an onboard SOFC system [2]. Thus, the conversion of the chemical energy of a liquid biofuel into electricity brings outstanding advantages to overcome the limitations of both hydrogen and batteries.

Taking the advantage of the high operating temperature ($\geq$600 °C), SOFC systems can be directly fed with liquid fuels, such as bioethanol. In this case, H_2 and CO/CO_2 are obtained through bioethanol reforming without the use of an external reformer, which reduces both the complexity and the cost of the system. Furthermore, the fuel cell electrochemical reaction consumes the H_2 formed at the anode side, which increases the conversion of bioethanol and the overall efficiency of the process [3,4].

Despite the advantages of internal reforming in SOFC systems, problems related to the direct conversion of primary fuels (hydrocarbon and alcohols such as methane and ethanol) in such high-temperature devices still hamper a widespread use of this technology. One of the main challenges is the dehydrogenation of the fuel at the metal particles of the standard nickel-based anode cermet. The complex reactions taking place at the anode of SOFCs running on carbon-containing fuels involves various pathways that usually result in irreversible degradation of the device by carbon deposits.

The use of carbon-containing fuels in SOFC is possible, when it is added an agent of oxidation (usually, water) to the stream to avoid the thermodynamic conditions for carbon formation [5,6]. Nevertheless, such strategy requires large amounts of water and adds complexity to the system design, significantly reducing its efficiency [7]. A second approach is to change or replace the traditional anode, the Ni/YSZ cermet. Several compounds have been suggested as alternative anodes, including different cermets (mainly zirconia- and ceria-based), and single-phase ceramic compounds, such as chromite-manganites and titanates [5,8]. However, finding an alternative material to the Ni/YSZ cermet that combines good catalytic and electrochemical properties, along with stability, compatibility, and low cost, remains a challenge. Currently, no alternative anode has outperformed the standard Ni/YSZ cermet on hydrogen. Therefore, an anode design that separates the catalytic and the electrochemical reactions in different anodic functional layers has been considered as a promising approach [9–12]. By separating the anode reactions in different layers, it is possible to use the Ni/YSZ anode for hydrogen combined with an appropriate catalyst for the targeted fuel. An increasing number of reports have confirmed that SOFC technology is expanding its multi-layer component design to the anode to enable the operation on available fuels other than hydrogen [12–16]. As recent examples, protective layers of ceria-based catalysts [14] and Ni-perovskite with FeOx core-shell nanoparticles [17] were used to coat standard Ni/YSZ anode for direct ethanol SOFC.

The use of the catalytic layer prevents the formation of carbon deposits on the cermet, since the fuel is converted into H_2 and CO before reaching the Ni-YSZ anode.

The increase of the nickel dispersion by reducing Ni loading of anodes is an additional strategy to suppress the formation of coke [16]. However, adequate conductivity for SOFC cells is not achieved when anodes with Ni content below 30%, prepared by traditional methods, are used. Thus, some authors [18–20] have reported the use of alternative preparation methods in order to obtain anodes with low Ni content, which are active, stable and with high conductivity to SOFC applications. Moddaferi et al. [19] observed no carbon deposition in Ni based anodes with low metal content (5 wt% Ni and 5 wt% Ru) prepared by a hydrothermal method during oxidative steam reforming of propane under SOFC operation conditions. Cermets with highly dispersed Ni particles (14 vol.%) synthesized by a net shape method were reported to display electrical conductivity comparable to that observed for the cermet with 35 vol % of Ni synthesized by a traditional technique [20]. Such method was used in Ni/CeGd anodes with 14 vol % of Ni prepared by a hydrothermal method for fuel cells operating with dry ethanol with good stability [18].

As an additional property to avoid carbon formation and increase the conductivity, several works have reported redox

supports, such as ceria-based as the ceramic phase for the SOFC anode [16,21–26]. Ceria is known to stabilize, on its surface, well-dispersed noble metals, promoting water-gas shift and hydrocarbon reforming reactions [27–29]. Ceria presents the ability to act as a store of oxygen due to its low reduction potential [30]. Under reducing atmosphere, CeO_2 is reduced with the formation of oxygen vacancies and small polarons represented by the Kröger-Vink notation [31] in Eq. (1),

$$2\,Ce_{Ce}^{\times} + O_O^{\times} = 2\,Ce_{Ce}^{\prime} + V_O^{\bullet\bullet} + \frac{1}{2}\,O_2 \quad (1)$$

However, at T > 1173 K ceria loses its porous structure, inducing a dramatic reduction in the catalytic activity ascribed to a decrease of the active phase dispersion. Various attempts have been proposed to optimize the activity and stability of ceria-based catalyst by adding cations such as Gd^{3+}, Y^{3+}, Zr^{4+}, Nb^{5+}. However, it should be pointed out that, in spite of a rather large number of experimental data, the role of these dopants on the catalytic properties of ceria is still under debate [32].

Cerium-zirconium based oxides of various compositions have been widely studied for utilization as catalytic support in three-way catalysts technology [33] and in SOFC operating on various compounds [33,34]. Obviously, considering an ideal solid solution, doping ceria with Zr^{4+} ions does not change the defects concentration. Various explanations for the observed enhanced properties have been proposed. The substitution of Ce^{4+} for the smaller Zr^{4+} ion induces a distortion of the ceria framework. The resulting displacement of oxygen atoms from their ideal positions induces a lowering of the energy barrier for oxygen migration and, consequently an increased oxygen mobility [35–41] and improving the surface area stability [42,43]. According to Janvier et al. it is not valid to consider the solid solution ($Ce_{1-x}Zr_xO_2$) a thermodynamically ideal solution as a dilute solution of point defects in the oxide [44]. They showed that the oxygen exchange between the gas phase and the solid is favored on the surface region. Moreover, the addition of zirconium ions would decrease the rate of surface loss at high temperature owing to the formation of solid solution between zirconium and trivalent cerium ions. Differently, trivalent cations dopants, such as Gd^{3+}, Y^{3+} or Sm^{3+}, in CeO_2 enhance the catalytic activity through the production of anion vacancies [45], according to Eq. (2):

$$Gd_2O_3 \rightarrow 2\,Gd_{Ce}^{\prime} + 2\,O_O^{\times} + V_O^{\cdot\cdot} \quad (2)$$

The comparison of the kinetics of hydrocarbon oxidation on pure and Sm-doped ceria has been reported [46]. No difference between the rate of oxidation of methane and ethane has been observed. In addition, the rate of propane and n-butane formation was significantly higher on ceria compared to Sm-doped ceria [47,48]. The main conclusions pointed out that the reaction rates are affected by the mechanism, which, in turn is strongly dependent on both the temperature and the state of the C–H bonds, and that catalytic reactivity of ceria support is not necessarily enhanced by trivalent dopant cations.

Another possibility is doping ceria with M^{5+} ions, such as Nb^{5+}. In this case, theoretically, without considering defect associations, three doping reactions can be considered:

$$Nb_2O_5 + V_O^{\cdot\cdot} \rightarrow 2\,Nb_{Ce}^{\cdot} + 5\,O_O^{\times} \quad (3)$$

$$Nb_2O_5 + 2\,Ce_{Ce}^{\times} \rightarrow 2\,Nb_{Ce}^{\cdot} + 4\,O_O^{\times} + \frac{1}{2}\,O_2 + 2\,Ce_{Ce}^{\prime} \quad (4)$$

$$Nb_2O_5 \rightarrow 2\,Nb_{Ce}^{\cdot} + 4\,O_O^{\times} + O_i^{\cdot\cdot} \quad (5)$$

Doping with Nb^{5+}, according to Eq. (3), fills oxygen vacancies and is associated with a lowering of the ionic conductivity. Reaction (4) induces a noticeable increase of the electronic conductivity of small polaron type for charge compensation, whereas reaction (5) induces a small increase of the ionic conductivity ascribed to the low mobility of interstitial oxygen ions. The relation between electrical conductivity, thermogravimetric measurements and defect structure has been studied by various authors [49–53]. It has been demonstrated that, under reducing conditions, reaction (4) is prevalent, while at low temperature and high oxygen partial pressure Nb^{5+} ions are incorporated into CeO_2 lattice by simultaneous reduction on some Ce^{4+} to Ce^{3+} and formation of oxygen interstitials according to reactions (4) and (5). The reactivity of Gd- and Nb-doped ceria for methane conversion to syngas was previously compared [51,54]. It has been concluded that Gd-doping has little effect and that Nb-doping decreases the reaction rate. However, some authors [54] have reported that ceria doped with is the most efficient to remove the carbon formed.

There are considerably fewer reports on the direct utilization of ethanol in SOFC as compared to methane, and some have proposed the use of cerium-zirconium and cerium-gadolinium based anodes [17,55,56]. Nonetheless, systematic studies about the effect of the dopant type on the performance of SOFC cells fed directly with ethanol are missing. Da Silva et al. [57] evaluated the behavior of Ni/CeO_2 cermets doped with Gd, Y, Pr, Zr and Nb as catalysts for the ethanol. However, the calcining temperature (1073 K) used for such catalysts was lower than that usually needed for ceramic processing of SOFC layers and the electrochemical characterization of devices was lacking. Thus, the goal of the present study is to investigate how dopants affect the catalytic properties of Ni/doped-ceria cermets and the role of such catalyst on the stability of direct ethanol SOFC.

Cermets containing with 18 wt% of Ni supported on ceria doped with Gd, Zr, Pr, Y or Nb were prepared and characterized [57]. Temperature programmed reduction (TPR) and *in situ* X-ray diffraction (XRD) analyzes were carried out to determine the reducibility of the samples and to evaluate the loss of catalyst activity and the changes in the catalyst crystalline structure during the reduction and the ethanol reactions. Post reaction thermogravimetric (TG), temperature programmed oxidation (TPO) and scanning electron microscopy (SEM) analyzes were carried out to investigate the quantity and nature of the carbon deposited during the decomposition of ethanol. The detailed catalytic characterization was used to select the most promising compositions for testing in SOFC single cells running on internal ethanol reforming. Stability tests showed that direct ethanol SOFCs can run using ceria-based catalysts for more than 100 h of continuous operation without degradation due to carbon deposits.

Experimental

Catalyst preparation and characterization

The cerium-based supports were synthesized using a method reported elsewhere [17,50]. Cerium (IV) ammonium nitrate and the nitrate of dopant (Y, Nb, Gd, Zr) were used as precursors. The co-precipitation of the hydroxides of dopants and cerium was carried out by addition of excess of ammonium hydroxide to a solution containing water and the precursors of cerium and dopants (Ce/dopant molar ratio = 9.0). Next, the precipitates obtained were heated in an autoclave to 453 K for 4 h. After washing with distilled water, a calcination of the samples at 573 K for 2 h were carried out using a muffle furnace.

Aiming at a high dispersion of the metallic phase to obtain cermet anodes with good electrical conductivity, while minimizing possible carbon deposits, Ni (18 wt%) was added to the ceria supports by wet impregnation of an aqueous solution of nickel nitrate [18,20]. After impregnation and drying at 393 K, the samples were heated at 1473 K in a muffle following a temperature schedule previously described elsewhere [17,50]. Such relatively high temperature was chosen to resemble the temperature required for ceramic processing of SOFC layers. Thus, the comparison of catalyst performance for both fixed-bed reactors and SOFC single cell tests are based on materials with similar microstructural properties. Then, four samples were obtained: Ni/CeGd; Ni/CeY; Ni/CeZr; Ni/CeNb.

For a more complete understanding of the activity and carbon deposition resistance of the samples, along with the catalyst composition, various parameters resulting from the synthesis method [58] have to be considered. Parameters such as BET surface area, the particle size of both the metallic active phase and ceria support, and the interaction between the metal and the support were accessed for the prepared materials.

A Micromeritics ASAP 2020 analyzer was used to measure the surface areas of the samples by adsorption of N_2 at 77 K.

In situ XRD analyses were carried out during the reduction treatment from 298 to 1123 K and decomposition of ethanol (ED) at reaction temperature of 1123 K/1 h. The Scherrer equation was used for the calculation of Ni crystallite size after reduction and after ED reaction. The equipment and analysis conditions used are described in detail elsewhere [57]. The degree of reduction of the samples was obtained (Eq. (6)) using the total amount of H_2 consumed during TPR analyses and the theoretical amount of H_2 consumed for the complete reduction of nickel species present in the samples.

$$\text{reduction degree (\%)} = \frac{\text{total amount (mols) of } H_2 \text{ consumed}}{\text{theoretical amount (mols) of } H_2 \text{ consumed}} \times 100 \quad (6)$$

Temperature programmed reduction (TPR) runs were performed to study the reducibility of the catalysts. The samples were initially pretreated at 673 K under air flow, and the TPR analyses were carried out under a hydrogen/argon mixture (30 mL min^{-1}) containing 1.5% of hydrogen from 673 to 1273 K (10 K/min). The degree of reduction of the samples was obtained (Eq. (6)) using the number of moles of hydrogen consumed during the reduction and the theoretical number of moles of H2 consumed for the total reduction of Ni present in the sample.

The quantity of carbon formed over the catalysts after decomposition of ethanol was determined by TG experiments. The analyses were carried out using a Shimadzu (TG-60) equipment. The weight variation of the used catalyst (10 mg) was measured during the heating of the samples from 298 to 1273 K under air flow.

The spent catalysts were characterized by scanning electron microscopy (SEM) analyses. Before SEM analyzes, the materials were submitted to the same reduction treatment described in XRD analyzes. The equipment and analysis conditions used are described elsewhere [57].

Ethanol conversion in a fixed-bed reactor (CR)

Ethanol decomposition (ED) and steam reforming (SR) of ethanol reactions were carried out in quartz reactor at 1123 K and a pressure of 1 atm. In the case of SR of ethanol, it was used a H_2O/ethanol molar ratio of 3.0 that corresponds to the stoichiometric according to the reaction (Eq. (7)):

$$C_2H_5OH + 3H_2O \rightarrow 2\,CO_2 + 6H_2 \quad (7)$$

A catalyst mass of 20 mg of sample was used to study the loss of catalytic activity in a short run time. In addition, SiC was used as a diluent with a SiC mass/catalyst mass of 3.0. The products obtained during the reaction were analyzed by a gas chromatography (Micro GC Agilent 3000 A). More details on the equipment, pretreatment of samples and reaction conditions can be found in the literature [57].

The conversion of ethanol ($X_{ethanol}$) and the selectivity to the products (S_x; where x = hydrogen, carbon monoxide, carbon dioxide, methane, acetaldehyde or ethylene) were calculated according the equations presented below:

$$X_{ethanol} = \frac{(mols\ of\ ethanol)_{fed} - (mols\ of\ ethanol)_{exit}}{(mols\ of\ ethanol)_{fed}} \times 100 \quad (8)$$

$$S_x = \frac{amount\ of\ x\ product\ formed\ (mols)}{total\ amount\ of\ products\ formed\ without\ water\ (mols)} \times 100 \quad (9)$$

Fuel cell fabrication

To study the properties of the catalyst aiming at the fabrication and test of fuel cells some parameters were studied.

The sintering behavior of die-pressed ceramic samples was investigated by dilatometry in a Netzsch DIL 402C. The linear retraction of green compacts was measured during heating (5 K/min) from room temperature to 1673 K under air flow.

The electrical conductivity of cylindrical pellets of both doped-ceria and NiO/doped-ceria composites sintered at 1723 K were evaluated. Silver paste contact pads were deposited on the parallel surfaces of samples and cured at 873 K. The electrical properties were determined by impedance spectroscopy measurements using a Solartron1260 with ac amplitude signal of 100 mV in the 10 MHz-1 Hz frequency

range. Impedance measurements were performed in the temperature range of 298–1073 K under flowing synthetic air. The total electrical resistance (dc resistance) was determined by the intercept of the low frequency end with real axis of the impedance diagrams. The temperature dependence of the dc electrical resistance was plotted and linear fits using Arrhenius equation were used to calculate the activation energy for the electrical transport.

Electrolyte-supported single cells were prepared using yttria (8 mol%)-stabilized zirconia (Tosoh, Japan). The yttria-stabilized zirconia (YSZ) cylindrical substrates were sintered at 1873 K, reaching apparent density >95% and typical final dimensions 18 mm diameter and ~0.5 mm thickness.

Two configurations of electrolyte-supported single cells were studied (Fig. S1), similarly as described elsewhere [18]. The first one was the standard (cathode/electrolyte/anode) electrolyte-supported fuel cell (ESFC). In the ESFC, the anode functional layer (AF), at the interface with the YSZ electrolyte, was the Ni/YSZ (40/60 vol.%), and the Ni/doped-ceria was the outer current collector layer (CC). Electrode layers of single cells were deposited by spin-coating using suspensions based on terpineol and ethyl cellulose [14]. The AF layer was deposited and sintered at 1723 K for 2 h in air, followed by the deposition of NiO/doped-ceria CC layer. $La_{0.65}Sr_{0.3}MnO_3$ (LSM) cathodes were deposited over a functional YSZ/LSM (50/50 wt %) composite layer deposited onto the electrolyte. Both the cathode and the anode CC layers were co-sintered at 1423 K in air for 1 h. The current collection at the anode side of the ESFC was an Au mesh attached to the anode CC layer with Au ink, followed by curing at 1073 K.

The second configuration of single cells was the electrolyte-supported fuel cell with catalytic layer (CLFC) [18,58] deposited over the anode. In CLFC configuration, the single cell was composed by the standard Ni/YSZ anode layers (AF 40/60 vol.% and CC 60/40 vol.%), and the Ni/doped-ceria catalytic layer was deposited as an additional outer layer [9,10,14,18] In the CLFC, anode current collection was made in the CC layer and the catalytic layer has no influence on the electrical properties of the single cell. Such a catalytic layer protects the Ni/YSZ anode from the direct contact with the fuel and promotes the ethanol reforming [10,14]. The CLFC single cell fabrication followed the same procedures of the ESFC, with both Ni/YSZ anode AF and CC layers sintered at 1723 K. Thus, prior to the catalytic layer deposition, a gold suspension (>70 wt% of Au, by Fuel Cell Materials) was used to: i) paint a contact mesh on the surface of the CC layer and ii) to glue a gold wire ring placed along the perimeter of the CC surface. Such an Au wire was used as the electrical contacts of the specimen for the electrochemical characterization. Then, the Ni/doped-ceria catalytic layer was deposited onto the CC layer and gold contact by spin coating and fired at 1173 K in argon flow for 1 h. For both ESFC and CLFC, a Pt mesh was applied to the surface of the cathode by using a Pt ink. The Pt current collector was cured in air at 1073 K.

Fuel cell testing

The single cells have an active electrode area of 0.78 cm^2 and were sealed on the tip of an alumina tube using a refractory cement (Aremco 552). The alumina tube with the sealed sample was inserted into a resistive horizontal tube furnace and connected to the metallic heads of a homemade test station with four Pt wires for electrical contacts. Temperature was measured by a thermocouple (type K) placed close to the cathode side and gas flow rates were set by mass flow controllers, both interfaced to a microcomputer. The single cell was heated up to 1123 K under N_2 flow and then changed to hydrogen (3 vol.% H_2O), with 50 mL min^{-1} flow rate, for anode reduction and system stabilization. During all fuel cell tests, synthetic air was flown (50 mL min^{-1}) to the cathode. Polarization and impedance spectroscopy data were taken during the initial operation on hydrogen. At 1123 K, the fuel cell was polarized at 0.6 V and hydrogen was switched to dry ethanol. The ethanol was vaporized and carried by bubbling N_2 (42 mL min^{-1}) through a saturator containing anhydrous ethanol at 313 K to obtain a gas composition of ~17% of ethanol in nitrogen, with total flow (N_2+ethanol) of ~50 mL min^{-1}. This ethanol concentration is set to keep the theoretical number of electrons constant for both fuels: hydrogen (100%) and ethanol (17%) [10,14]. To evaluate the stability for direct (dry) ethanol conversion, the single cells were continuously operated for different times on stream (TOS) while the current density (i) at fixed cell voltage of 0.6 V was measured as a function of the time. The electrochemical characterization was performed during cell operation under hydrogen and the ethanol stability tests using a Zahner IM6 Electrochemical Workstation. Polarization measurements under H_2 were taken from OCV to 0.2 V, with a resolution of 15 mV and a delay time of 1 s. During stability test under ethanol the potential range of the *i* x V curves was limited in the 0.6 V–0.2 V range to ensure the water generated by the electrochemical oxidation of hydrogen. Impedance spectroscopy data was collected under polarization at 0.6 V, with 10 mV ac amplitude in the 100 kHz –1 Hz frequency range. Impedance diagrams were deconvoluted using an equivalent circuit model (Fig. S11) described elsewhere [17,59]. The stability of fuel cells running on ethanol was verified in duplicate; at least two samples of each ceria dopant composition and fuel cell configuration (ESFC and CLFC) were tested. After fuel cell stability tests, SEM analyses of the fractured surfaces of the anode were carried out to examine possible carbon deposits.

Results and discussion

Characterization of the catalysts

All catalysts calcined at 1473 K presented a low surface area (<10 m^2/g) because of the high calcination temperature, in agreement with previous Ni/CeGd samples (8 m^2/g) prepared in the same conditions used in this study [18].

The XRD patterns obtained for samples after calcination are shown in Fig. 1. The diffraction lines of a cubic cerium oxide phase (ICSD 34-394) and oxide of nickel (JCPDS 24018) were observed for all samples. Comparing the 2θ positions of diffraction peaks of doped samples with that of CeO_2, a displacement of the diffraction peaks to lower 2θ was observed for Ni/CeGd, while the diffraction lines were shifted to higher 2θ values for Ni/CeZr, Ni/CeY and Ni/CeNb. These

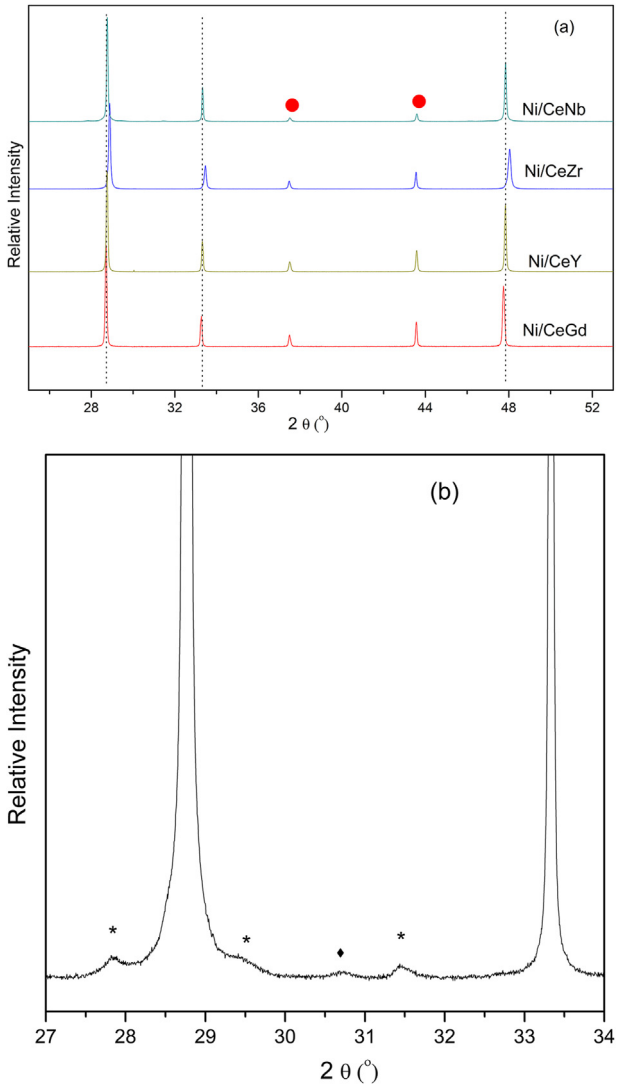

Fig. 1 – XRD analyses for (a) samples after calcination and (b) Ni/CeNb sample between 2θ = 27–34°: (- - -) CeO_2; (●) NiO; (*) $CeNbO_4$, (♦) $NiNb_2O_6$.

shifts were more significant for the samples containing Zr and Gd and were associated to contraction or expansion of the ceria lattice, respectively. The ceria lattice parameter (*a*) obtained for calcined samples (Table 1) showed that doping ceria with Gd^{3+} led to an increase of the lattice constant, while the addition of Y^{3+}, Zr^{4+} and Nb^{+5} reduced the lattice parameter in comparison to the reported lattice parameter of CeO_2 (5.412 Å) [60–62]. The lattice parameter dependence on the ionic radius of dopants in solid solutions of ceria with a fluorite type structure is well described and similar features were previously reported [63–65]. In the case of Zr^{4+} (0.084 nm) and Nb^{5+} (0.069 nm), which have ionic radius smaller than Ce^{4+} (0.097 nm), it was observed a contraction of ceria lattice. The opposite effect was determined for Gd^{3+} (0.105 nm) doping that results in larger ceria lattice parameter. However, for the sample doped with Y^{3+}, a contraction was observed, despite of Y^{3+} having a larger ionic radius (0.102 nm) than Ce^{4+}. This behavior was previously observed for dopants with ionic radius smaller than that of the Gd^{3+}, such as Yb^{3+}, Ho^{3+} Er^{3+}, and Y^{3+}, and ascribed to both electrostatic and steric effects caused by interactions between oxygen vacancy, cerium and the dopant [65–69].

Table 1 – Values of CeO_2 lattice parameter obtained for samples after calcination at 1473 K and after reduction at 1023 or 1123 K (Miller index used (111)).

Sample	Lattice parameter (Å)		
	After Calcination At 1473 K	After reduction at 1023 K	After reduction at 1123 K
Ni/CeGd	5.4164	5.4684	5.4779
Ni/CeY	5.4062	5.4628	5.4824
Ni/CeZr	5.3843	5.4577	5.4705
Ni/CeNb	5.4044	5.4515	5.4811

Regarding Ni/CeNb, the lines corresponding to monoclinic phase of $CeNbO_4$ (PDF 01-072-0905) and nickel niobate phase (PDF 32-0694 and ICSD 37-213) were detected (Fig. 1b).

In situ XRD analyses carried out during reduction for Ni/CeNb and Ni/CeZr are shown in Fig. 2. The XRD patterns of the other catalysts are shown in the supplementary information (Figs. S2 and S3).

For all catalysts, the values of 2θ observed for diffraction lines corresponding to CeO_2 cubic phase decreased, when the reduction temperature was increased. The shift observed up to 600 K is attributed to a lattice expansion that occurs when temperature is increased [57]. However, at higher temperatures, this shift is also associated with the formation of oxygen vacancies and Ce^{3+} cations due to the reduction of CeO_2 because ionic radius of Ce^{4+} (0.97 Å) is smaller than that of Ce^{3+} (1.14 Å). A comparison of XRD patterns obtained for ceria-doped samples showed that this displacement was more pronounced for the catalyst containing Zr. The shift of these lines upon reduction decreased in the order: Ni/CeZr > Ni/CeNb ≈ Ni/CeY > Ni/CeGd. These results confirm that the promotional effect on ceria reducibility was more significant using Zr as dopant.

Regarding Ni/CeNb sample (Fig. 2b), the increase of reduction temperature led to a decrease in the intensity of the lines related to monoclinic phase of $CeNbO_4$ and $NiNb_2O_6$ whereas the lines associated with tetragonal phase of $CeNbO_4$ was observed. At 1123 K, the lines of $NiNb_2O_6$ and monoclinic phase of $CeNbO_4$ were no longer detected. Previous study [70] indexed $CeNbO_4$ with a monoclinic structure at room temperature. However, when $CeNbO_4$ was heated under air or vacuum, the tetragonal phase was detected above 573 K.

Tables S1 and S2 (Supplementary information) report the CeO_2, NiO and Ni^0 crystallite sizes obtained after calcination at 1473 K and during the reduction under H_2 from 298 to 1123 K. Relatively large crystallite sizes calculated for both ceria (80–130 nm) and NiO (84–129 nm) are attributed to the high calcining temperature. The reduction at 1123 K led to an increase of average particle size of CeO_2 for the samples with Zr and Gd. On the other hand, no significant changes were observed in average particle size of CeO_2 for the catalysts containing Y and Nb. Regarding nickel, all samples reduced at 1023 K exhibited large metallic Ni crystallites (89–118 nm). The catalysts doped with Zr and Nb presented the largest and smallest metallic Ni crystallite size, respectively. A raise of the

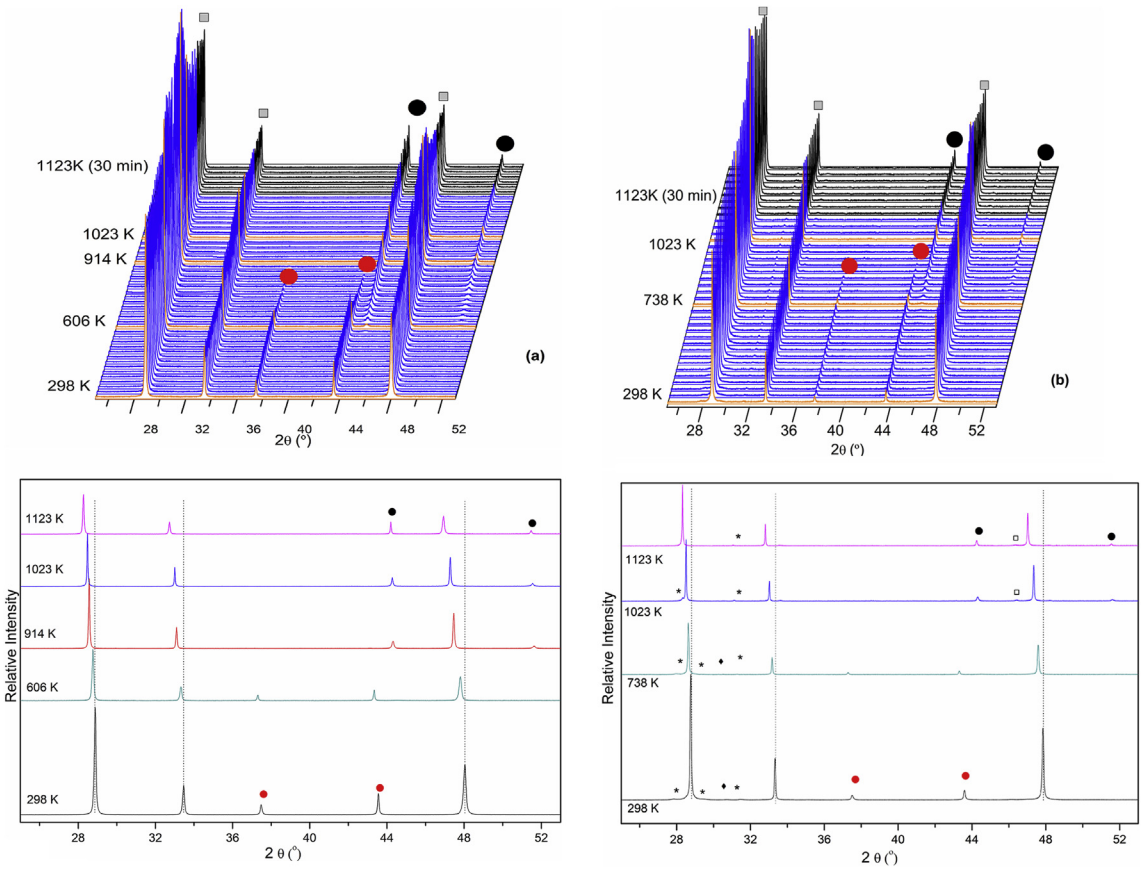

Fig. 2 – XRD analyses obtained during reduction for catalyst doped with (a) Zr and (b) Nb; the orange curves corresponding to diffractograms at selected temperatures shown in the bottom pannels. (—, ■) CeO_2, (●) NiO; (●) Ni, (*) tetragonal $CeNbO_4$, (❑) monoclinic $CeNbO_4$ (♦) $NiNb_2O_6$. (For interpretation of the references to color in this figure legend, the reader is referred to the Web version of this article.)

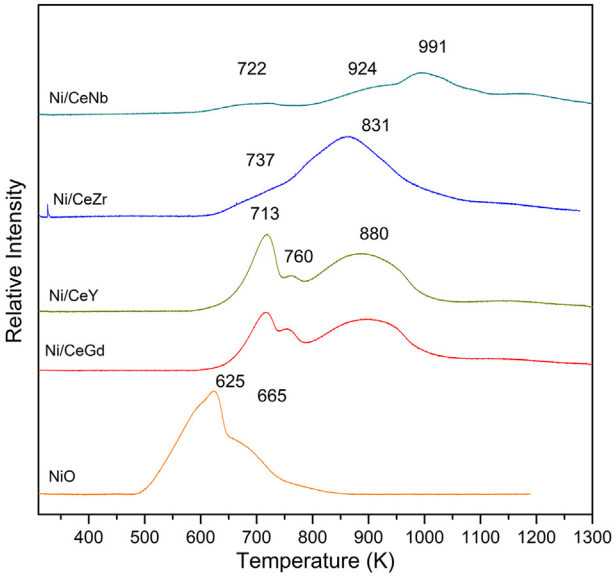

Fig. 3 – TPR profiles of calcined samples.

temperature of reduction to 1123 K caused to an increase in Ni^0 average particles size for all samples. The samples with Gd and Nb presented the larger metallic average particles size.

The TPR profiles for all calcined materials are presented in Fig. 3. It was also presented the TPR analysis of bulk NiO for comparison. The TPR profiles of Ni/CeGd and Ni/CeY were similar. Three reduction peaks at 713, 760 and 880 K were detected for these samples. For Ni/CeZr, there is only a shoulder at around 737 K, which is likely due to the large H_2 consumption with a maximum at 831 K. This broad peak at high temperature extends up to 1050 K for catalysts containing Gd, Y and Zr. A comparison between these results with those obtained *in situ* XRD analyses showed that the peaks of H_2 at temperature range of 713 and 880 K corresponding to the formation of Ni^0 due to NiO reduction. According to the previous reports [71,72], the H_2 uptakes at 713 and 737–760 K can be associated with the formation of Ni^0 from the reduction of bulk nickel oxide. The H_2 consumption at higher temperatures (880 K) corresponds to the reduction of nickel oxide particles that exhibit a stronger interaction with the support [72]. A comparison of TPR profiles obtained for catalysts containing Gd, Y and Zr showed that the Zr-doped sample exhibited the highest H_2 consumption at higher reduction temperatures.

Because the degree of reduction of samples doped with Gd, Y and Zr exceeded the value of 100% (Table 2), the peaks of H_2 consumption at 600–1300 K could be related to reduction of

Table 2 – H_2 consumption and degree of reduction of NiO calculated by TPR analyses.

Catalyst	H2 consumption μmol/gcat	Reduction degree (%)
Ni/CeGd	243	142
Ni/CeY	218	128
Ni/CeZr	264	155
Ni/CeNb	147	86

both nickel oxide and CeO_2 crystallites promoted by the presence of metal through hydrogen spillover [42,73].

Contrary to what was observed in the TPR analyses for samples containing Zr, Gd e Y, for the catalyst doped with Nb, it was detected small H_2 consumptions around 722 and 924 K. Additionally, a peak at high temperature (991 K) was observed. Moreover, the reduction of NiO was not complete (reduction degree of NiO = 86%). Some authors [74,75] reported that the low reducibility of Ni/CeNb catalysts could be assigned to the formation of a phase of $NiNb_2O_6$. The reduction of this phase occurs at temperatures higher than 773 K. Some works [76,77] showed that the H_2 consumption at high temperature in the TPR profile of niobia-promoted Rh/SiO_2 catalyst is due to the presence of a $RhNbO_4$ phase. In this work, XRD analysis of Ni/CeNb detected the presence of a $NiNb_2O_6$ phase after calcination. In addition, a Ni/CeNb sample showed H_2 consumption in the TPR analyzes in the same regions as the $NiNb_2O_6/CeO_2$ catalyst. This catalyst also exhibited the formation of CeO_2, $CeNbO_4$, NiO and $NiNb_2O_6$, after calcination, as revealed by XRD analysis [57]. Herein, the results observed indicate that the peaks of H_2 uptake at low temperatures can be related to NiO reduction. Moreover, the H_2 consumption at high temperatures can be related to the reduction of $NiNb_2O_6$ phase.

ED and SR of ethanol in a fixed-bed reactor

In this section, the decomposition and steam reforming of ethanol in a fixed-bed reactor and the characterization of the catalysts after reactions are presented.

ED and SR of ethanol

ED at reaction temperature of 1123 K was carried out without catalyst (Fig. 4a). At the beginning of the reaction, ethanol was consumed completely. It was also observed the formation of hydrogen, carbon monoxide, carbon dioxide, methane and small quantities of ethylene.

In the presence of the catalyst, the ethanol conversion remained constant during 28 h time on stream (TOS), as shown in Fig. 4b and c for Ni/CeZr and Ni/CeNb, respectively. The same results were observed for other catalysts (Fig. S4a–b, Supplementary information). The presence of the catalysts led to a higher production of H_2 and a lower formation of ethylene. In the first 4 h of reaction, a decrease in the H_2 production and an increase in the selectivity to carbon monoxide, methane and ethylene were detected. At the end of the reaction (28 h TOS), the selectivities were around 45, 30, 20 and 5-10% for H_2, CO, CH_4 and ethylene, respectively. It was observed that the type of dopant did not affect the conversion of ethanol conversion and the selectivities to products for ED at 1123 K. Taking into account the mechanism of ethanol reactions previously proposed [78], the products obtained indicate that the ethanol decomposition and dehydration reactions are taking place. Augusto et al. [18] showed the same results for decomposition of ethanol using Ni supported on cerium oxide doped with Gd as catalyst.

The effect of the addition of water to the feed was evaluated by SR of ethanol carried out at 1123 K. The values of conversion of ethanol and product distributions versus time on stream (TOS) for SR of ethanol (molar ratio of H_2O/ethanol molar ratio = 3.0) over catalysts containing Gd and Nb are presented in supplementary information (Fig. S5a–b). At the beginning of the reaction the ethanol was consumed completely. No loss of catalytic activity was observed during the reaction for both samples. The presence of the water in the feed stream led to an increase of the selectivity to H_2 and CO_2, whereas the production of CO and CH_4 decreased in comparison to the ED reaction. Furthermore, the formation of acetaldehyde and ethylene was not observed. No changes were detected in products distribution during the reaction. These results are in good agreement with the ethanol steam reforming reaction mechanism, indicating that the decomposition and reforming of ethanol reactions ($C_2H_5OH + 3H_2O \rightarrow 6H_2 + 2CO_2$) and reaction of water gas-shift were favored for the catalysts studied.

The design of an anode resistant to carbon deposition is one of the great challenges of SOFC powered by bioethanol. Some authors [8,79] reported that a deposition of large amounts of carbon was observed for SR of ethanol around 1173–1273 K over Ni/YSZ anode. The carbon deposition was assigned to the methane, ethane, and ethylene decomposition and to the occurrence of reaction of Boudouard.

In order to evaluate the causes for the loss of catalyst activity such as carbon formation and metal sintering, *in situ* XRD analysis during ED was performed. In addition, the SEM and TG analyses were carried out after ED and SR of ethanol.

In situ XRD during ED

The *in-situ* X-ray diffractograms obtained along the ED at reaction temperature of 1123 K for all catalysts are shown in Figs. S6 – S9 (Supplementary information). As previously described, the lines of Ni^0 and CeO_{2-x} phases were observed in the diffractograms for all samples after reduction. This indicates the partially reduction of CeO_2. For Ni/CeNb, the lines associated to tetragonal phase of $CeNbO_4$ were also observed. However, after 15 min of reaction, $CeNbO_4$ phase was no longer detected. In addition, a displacement of the lines corresponding to CeO_{2-x} phase to lower 2θ positions was observed during reaction for all samples. This displacement decreased in the order: Ni/CeZr > Ni/CeY > Ni/CeNb > Ni/CeGd. These results suggest that all samples underwent continuous reduction of ceria along the reaction and this effect was more important for Zr-doped ceria. Moreover, the lines related to NiO were not detected, indicating that crystallites of metallic Ni were not oxidized. The increase of reaction time led to a lattice parameter expansion. The hydrogen formed led to a reduction of Ce^{4+}, forming Ce^{3+} during the reaction (Table S3, supplementary information).

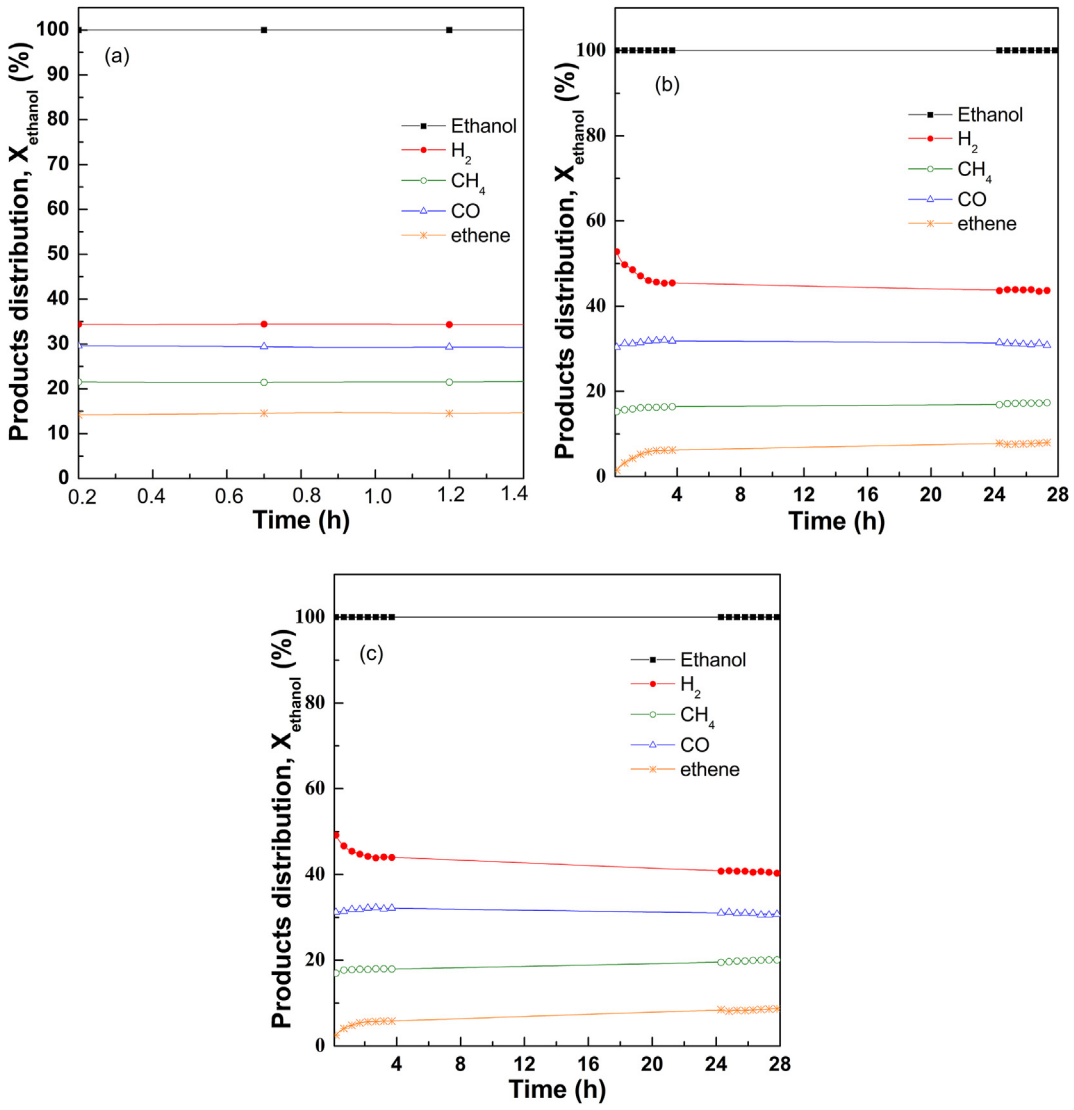

Fig. 4 – Product distribution and ethanol conversion for ED at 1123 K in the absence of catalysts (a) and over catalyst doped with Zr (b) and catalyst doped with Nb (c).

When the crystallite sizes of ceria calculated for the samples reduced at 1123 K were compared with those observed after 1 h of reaction (Table S1, supplementary information), it was observed that the CeO_2 crystallite size increased for Ni/CeY and Ni/CeNb. This effect was greater for the catalyst containing Y. On the other hand, for the Gd-doped sample, CeO_2 crystallite size decreased after reaction, whereas for Ni/CeZr, no significant changes were observed.

Concerning the Ni^0 crystallite (Table S2, supplementary information), an increase in crystallite size was only detected for Y-doped sample. For Ni/CeGd and Ni/CeNb, the Ni^0 crystallite size decreased after the reaction, and for Ni/CeZr, Ni^0 crystallite size remained practically unchanged.

Characterization of used catalysts

The results obtained in SEM analyses of the samples after ED are presented in Fig. 5. Carbon filaments were detected for all tested catalysts.

According to the mechanism proposed in the literature for ethanol reactions [78,80,81], ethoxy species and a bridging –OH group are formed by dissociative adsorption of ethanol on supported metal-based catalysts at low temperatures. With increasing temperature, ethoxy species can be dehydrogenated to acetaldehyde and acetyl species. At higher temperatures, the dehydrogenate species are converted to acetate species via support bound –OH groups. The acetate species can be decomposed to CO, CH_4 and carbonate, while the dehydrogenated species can be decomposed, producing H_2, CO and CH_x. When the rate of desorption of CH_x species (e.g. CH_4) is lower than the rate of formation of CH_x species catalyst deactivation occurs. In this case, the dehydrogenated of the CH_x species to form H and C takes place on metal surface. For Ni based catalysts, this highly reactive carbon species can encapsulate the metal particle or dissolve into the nickel lattice, forming nickel carbide. This is the first step for the nucleation and

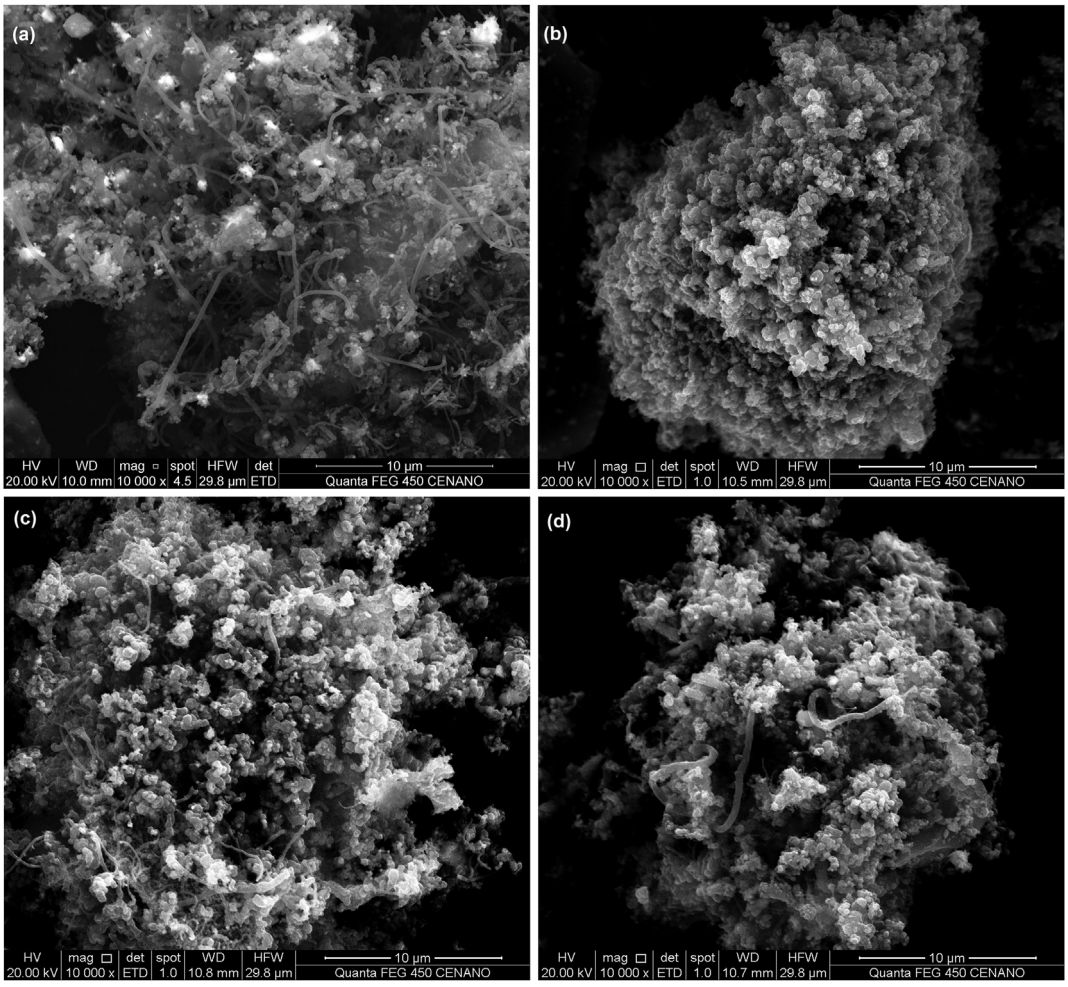

Fig. 5 – SEM images (x 5000) of catalysts obtained after ED carried out at reaction temperature of 1123 K for catalysts doped with: (a) Gd; (b) Y; (c) Zr; (d) Nb.

growth of carbon filaments The type of carbon formed also depends on reaction temperature [78]. At temperatures between 623 and 723 K, Ni particles are completely encapsulated by coke. On the other hand, when ethanol reactions were carried out at 773 or 823 K, carbon filaments were observed. At temperatures higher than 873 K, carbon deposition was not detected [17,78,80,81]. Such mechanism is possibly hampered in the studied Ni/doped-ceria due to the relatively large crystallite sizes resulting from the high processing temperatures.

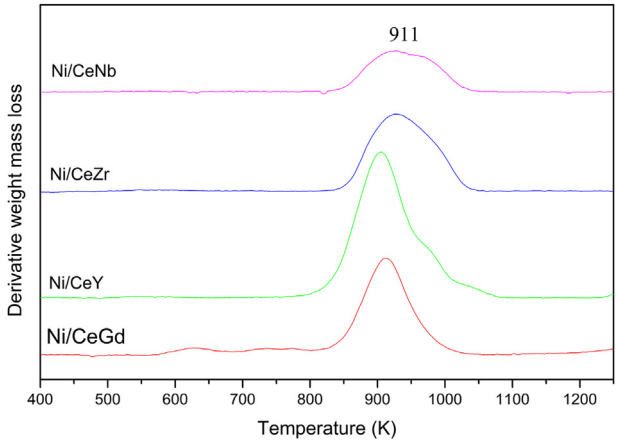

Fig. 6 – TPO profiles obtained by TG analyses for catalysts after ED carried out at reaction temperature of 1123 K.

Fig. 6 shows the TPO profiles obtained by TG analyses for catalysts after ED carried out at 1123 K. Only one broad peak from 830 to 1000 K was detected for all samples. These peaks at high temperatures in the TPO profiles of supported Ni-based catalysts after reactions of conversion of ethanol at temperatures around 773–873 K and higher than 873 K were attributed to the filamentous oxidation and graphitic carbon

Table 3 – Quantity of carbon formed on catalysts after ED carried out at reaction temperature of 1123 K (mg carbon/(g_{cat} h)).

Sample	Carbon formation rate (mg carbon/(g_{cat} h)
Ni/CeGd	4.5
Ni/CeY	5.0
Ni/CeZr	3.1
Ni/CeNb	1.8

oxidation, respectively [72,82–86]. Thus, SEM and TPO analyses carried out after ED reactions showed that the type of dopant has little effect on the morphology of carbon deposit. More significantly, the type of dopant had a clear influence on the total amount of carbon formed, as shown in Table 3.

The lowest (1.8 $mg_{carbon}/g_{cat}h$) and the highest rates of carbon formation were obtained over the catalysts doped with Nb and Y (5.0 $mg_{carbon}/g_{cat}h$). Moreover, Ni/CeGd and Ni/CeY exhibited a similar carbon formation rate.

Regardless of the type of carbon formed, the use of ceria-based oxides as a support can promote the removal of coke from the surface of supported metal catalysts [72,78,87–90]. In the case of carbon filaments, the nickel carbide formed at the first step for the nucleation and growth of filaments is oxidized by the oxygen supplied by the ceria support. The oxygen is transferred from the support to the metal at the metal-support interfacial perimeter. Therefore, a high oxygen storage capacity and a high area of the interface between metal and support are essential to obtain an adequate cleaning of the surface of metallic crystallite.

In this study, the Zr-doped Ce sample should exhibit a lower formation of carbon during ED, since Ni/CeZr showed a higher reducibility, as revealed by TPR and *in situ* XRD. However, similar quantities of carbon were obtained over catalysts containing Gd, Y and Zr. This result suggests that the increase of oxygen vacancy concentration did not inhibited the formation of carbon.

On the other hand, the presence of Nb in the ceria decreased the deposition of carbon. Such a result is possibly due to a combination of the charge compensation defects and a geometrical effect. Under low oxygen partial pressure, the cerium was reduced due to an electronic compensation that was produced by Nb-doping (Eqs. 4) and (5)). Such charge compensating defects result in increased electronic conductivity that was previously associated with an improved carbon oxidation in Nb-doped ceria as compared to Gd-doped sample [51]. Samples containing Nb exhibit a higher concentration of electronic carriers under oxidizing conditions that are available for the ionization of adsorbed oxygen species [48]. Thus, such oxygen species react with carbon formed, promoting the carbon removal on Nb-doped ceria [48]. Furthermore, previous studies proposed that the $RhNbO_4$ phase is formed during the calcination of Rh/SiO_2 catalyst promoted with Nb. At high reduction temperature, it was detected the formation of Rh and NbO_x species that are deposited on metal particles surface [76,77]. This effect decreased the reaction rate of hydrogenolysis of ethane. In this work, TPR and XRD analyses indicated the formation of a $NiNb_2O_6$ phase for Ni/CeNb catalyst. During the reduction of this phase, Ni particles covered by NbO_x patches could be formed, blocking some Ni active sites. This could lead to the occurrence of the so-called geometric effect that would affect those reactions requiring a large ensemble of atoms, such as the formation of carbon [91]. The carbon deposition rate for SR of ethanol is influenced by the metal particle size. The higher coke formation rate occurs on large metal particles due to the higher fraction of exposed terrace atoms [78,92]. The partial coverage of this terrace atoms by NbOx patches suppress the deposition of carbon.

Nevertheless, the presence of water in the feed avoided the deposition of carbon. The carbon formation was not detected over Ni/CeGd and Ni/CeNb after SR of ethanol, as revealed by SEM (Fig. S10) and TG analyses. Previous studies have shown that the mechanism of carbon removal was promoted in the presence of water that reduces the coke formation along the SR performed at high temperature reaction [55].

The Ni/doped-ceria catalysts here described complement previous studies in which Ni/CeGd cermets were investigated concerning the effect of the volume fraction of Ni [18]. In the present study, the main goal is to evaluate the effect of the dopant of cerium oxide, as the ceramic phase of Ni-cermets, considering both the catalytic and electrochemical properties for ethanol SOFC, to advance previous catalytic data on fixed bed reactors [57]. Thus, we have selected both the Zr^{4+} and Nb^{5+} dopants to study the Ni/doped-ceria cermets on fuel cells because such materials presented lower values of rate of

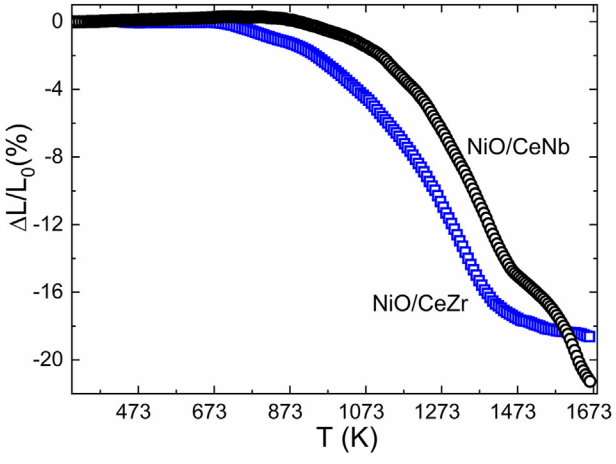

Fig. 7 – Dilatometric curves of the NiO/doped-ceria composite compacts.

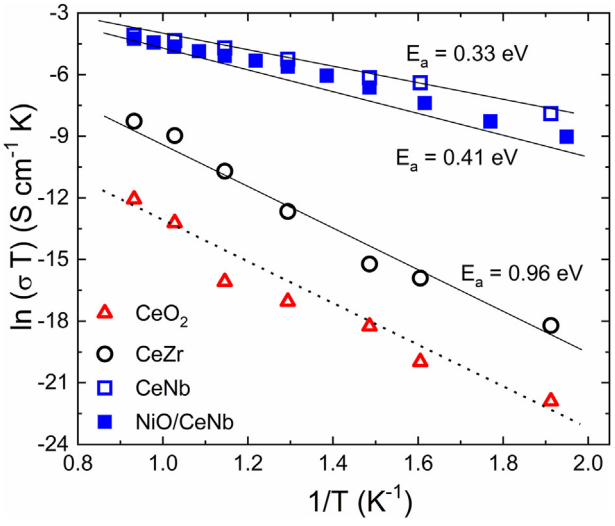

Fig. 8 – Arrhenius plots of the total conductivity extracted from the impedance diagrams of sintered pellets of (Nb and Zr)-doped ceria ceramics and Ni/CeNb. The straight lines correspond to the best Arrhenius fit. The conductivity of undoped ceria is shown as a reference.

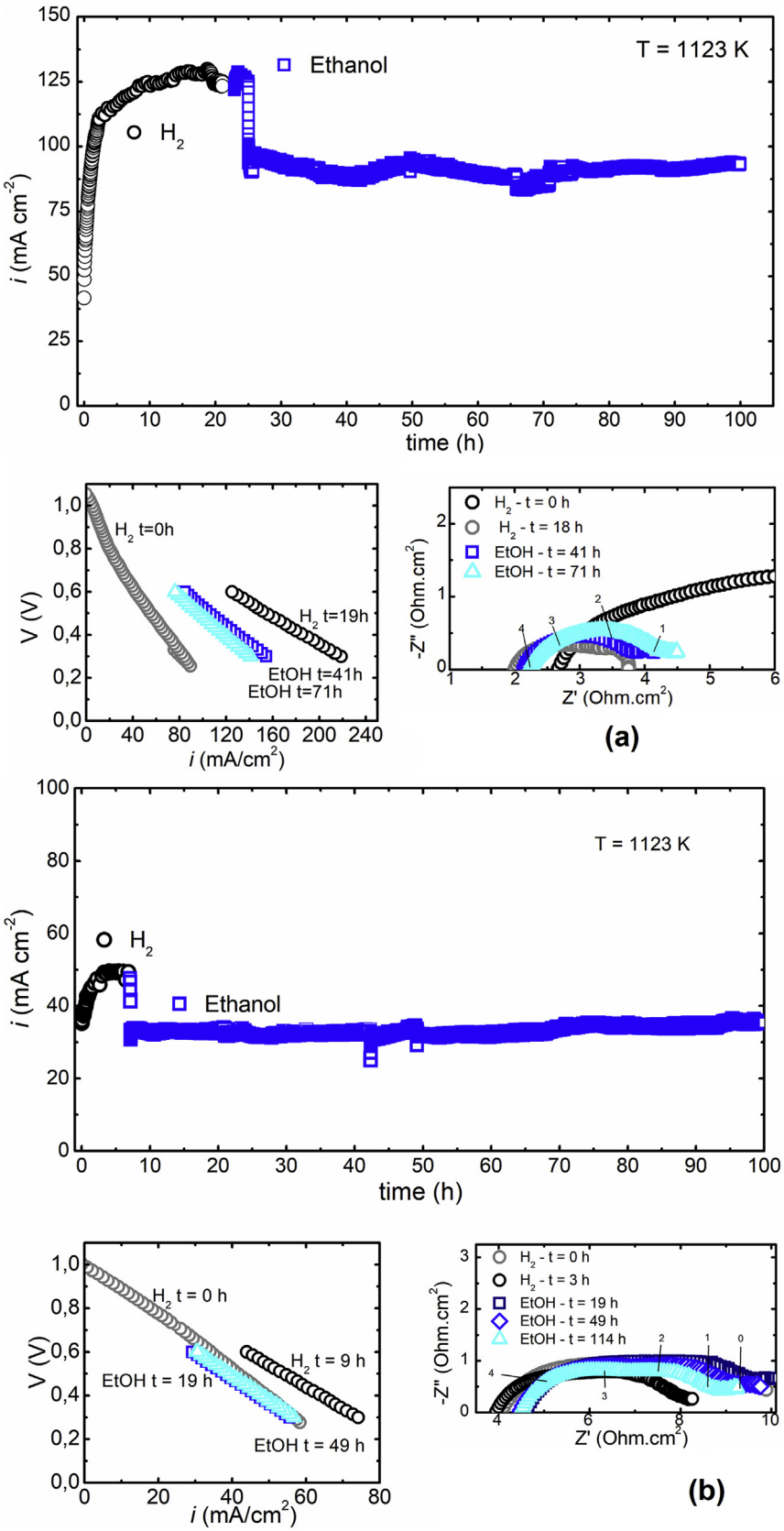

Fig. 9 – Durability tests at 1123 K and 0.6 V of fuel cells (ESFC) using (a) Ni/CeZr and (b) Ni/CeNb current collector anode layer. The corresponding impedance diagrams and i x V curves measured at different times during the durability tests are shown in the bottom panel.

coke formation during decomposition of ethanol, and, thus, they are the most promising compositions for direct ethanol SOFC.

Characterization of SOFC anodes

properties of the NiO/doped-ceria anode precursor

The sintering properties are essential parameters for the fabrication of SOFC anodes. The linear retraction as function of the temperature of NiO/doped-ceria green compacts is shown in Fig. 7. The Zr-doped ceria exhibited onset of linear retraction at around 723 K and the maximum retraction rate at around 1323 K. The retraction reaches a plateau at high temperature with a total retraction of approximately 18% at 1673 K. Nb-doped ceria showed a different behavior with both the onset of retraction and the maximum retraction rate shifted to 75 K higher than that of the CeZr sample, with a second maximum retraction rate at around 1628 K. Nb-doped ceria exhibited a total linear retraction close to 22%, but it has not reached the final sintering stage at 1673 K. Such features observed in the dilatometry data of Ni/CeNb are consistent with the presence of a secondary phase in the Nb-doped sample.

The dilatometry runs evidenced that different sintering temperatures used for fuel cell fabrication likely results in different microstructures of the studied cermets depending on the temperature used for fuel cell fabrication. Particularly, the current collector anode layer (CC) sintered at 1723 K, both Zr and Nb-doped samples may exhibit different final average particle size and porosity that may influence the electrolyte-supported (ESFC) fuel cell performance. Nonetheless, controlling such parameters was a hard task. Thus, we have adopted a standard procedure for fuel cell fabrication aiming to investigate preferably the stability of the fuel cell under ethanol rather than optimizing the electrochemical performance.

Fig. 8 shows the Arrhenius plots for both Zr- and Nb-doped ceria supports, CeO_2 as reference, and the NiO/CeNb anode precursor. All samples exhibited a thermal activated behavior that was fitted to an Arrhenius-type charge transport. Ideally, doping of ZrO_2 in CeO_2 may not promote the formation of oxygen vacancies, but increases the ionic conductivity of CeO_2. However, the substitution of Ce^{4+} for the smaller Zr^{4+} ion induces a distortion of the ceria framework that results in a displacement of oxygen atoms from their ideal positions inducing an increase in the mobility of oxygen and consequently an increase in electrical conductivity [47,48,93]. On the other hand, Nb doping leads to different charge compensation process that produce electronic defects resulting in a large electronic conductivity according to reaction (4) and ref [52,94]. The calculated activation energy E_a values reflect such features. Both ceria and CeZr samples have typical values for O^{2-} conductors (E_a0.9 eV). Differently, CeNb has a much lower E_a0.33 eV and higher total electrical conductivity, characteristics of mixed ionic-electronic conductor (MIEC) [52,95].

The results confirm that the ceria dopant has a pronounced effect on the electrical properties of the support, changing both the nature and the concentration of charge carriers. Adding a semiconducting second phase (NiO) in composites having an oxygen ion conductor as the matrix, as in NiO/ceria, it is expected to substantially increase the electrical conductivity and decrease the E_a values, as compared to the ionic conductor matrix [96,97]. In contrast, adding NiO to the CeNb, resulted in small changes in the electrical conductivity and E_a, evidencing the strong mixed ionic-electronic conductivity of CeNb sample. Such features will reflect in the electrical properties of the anodes and will be important for the direct ethanol fuel cell electrochemical characterization.

Direct ethanol fuel cell stability test

Firstly, both configurations of single cells (Fig. S1), the electrolyte-supported (ESFC) and the electrolyte-supported with catalytic layer (CLFC), were tested on H_2 for anode reduction and system stabilization, as shown in Fig. 9 and Fig. 10, respectively. After stabilization at 1123 K, all samples attained an OCV ~1.1 V, close to the theoretical value for H_2 (3 vol.% H_2O). Fuel cells were then polarized at 0.6 V and after ~20 h, H_2 was switched to dry ethanol (carried by N_2). The current density at 0.6 V was monitored while fuel cell was continuously operated for approximately 100 h for the stability tests on dry ethanol. Figs. 9 and 10 show the current density *i* as a function of the operating time at 1123 K along with the corresponding impedance diagrams and *i* x V curves taken during the test.

As a general trend, fuel cells were observed to increase the current output during the initial ~10 h of operation under hydrogen. In the CLFC samples (Fig. 10) the Ni/Ce(Zr,Nb) is the external catalytic layer and play no role on the electrical transport, whereas for the ESFC (Fig. 9) the Ni/Ce(Zr,Nb) is the current collection anode layer (CCL). Thus, CLFCs samples (Fig. 10) outperform the ESFC configuration (Fig. 9). Such a result is mainly related to the lower conductivity of the Ni/CeZr and Ni/CeNb cermets, with low Ni content (18 wt% Ni) used as CCL in ESFC. The metallic fraction of the studied cermet is considerably lower than that of the standard Ni/YSZ current collector composition (60 wt% Ni) used in the CLFC. Impedance spectroscopy data taken under polarization in hydrogen showed that both the ohmic and polarization resistances decrease within the initial 10 h. The observed decrease of the ohmic resistance agrees with a possible cathodic activation and a slow kinetics of the reduction of relatively dense anodic layers. Such a feature is possibly related to the low porosity of the anode layers attained during the fuel cell fabrication, as evidenced by measured apparent density of the samples after the dilatometry runs (Fig. 7). The Ni/doped-ceria samples showed a high sinterability with maximum retraction rate occurring at temperatures (1323 K), significantly lower than the one used for ESFC fabrication (1673 K). The low porosity of the Ni/doped-ceria CCL layer hinders the reduction of the anode during the initial hours of operation under hydrogen. Probably, as the NiO reduction develops, the anode porosity increases and promotes the enhancement of triple phase boundaries in the anode/electrolyte interface, decreasing the overall polarization resistance of the fuel cell.

By changing hydrogen to dry ethanol, a decrease in the performance was observed as a sharp drop (~35%) of the current density. It is important to consider that ethanol flow rate is reduced to a 1/6 of the hydrogen concentration to keep

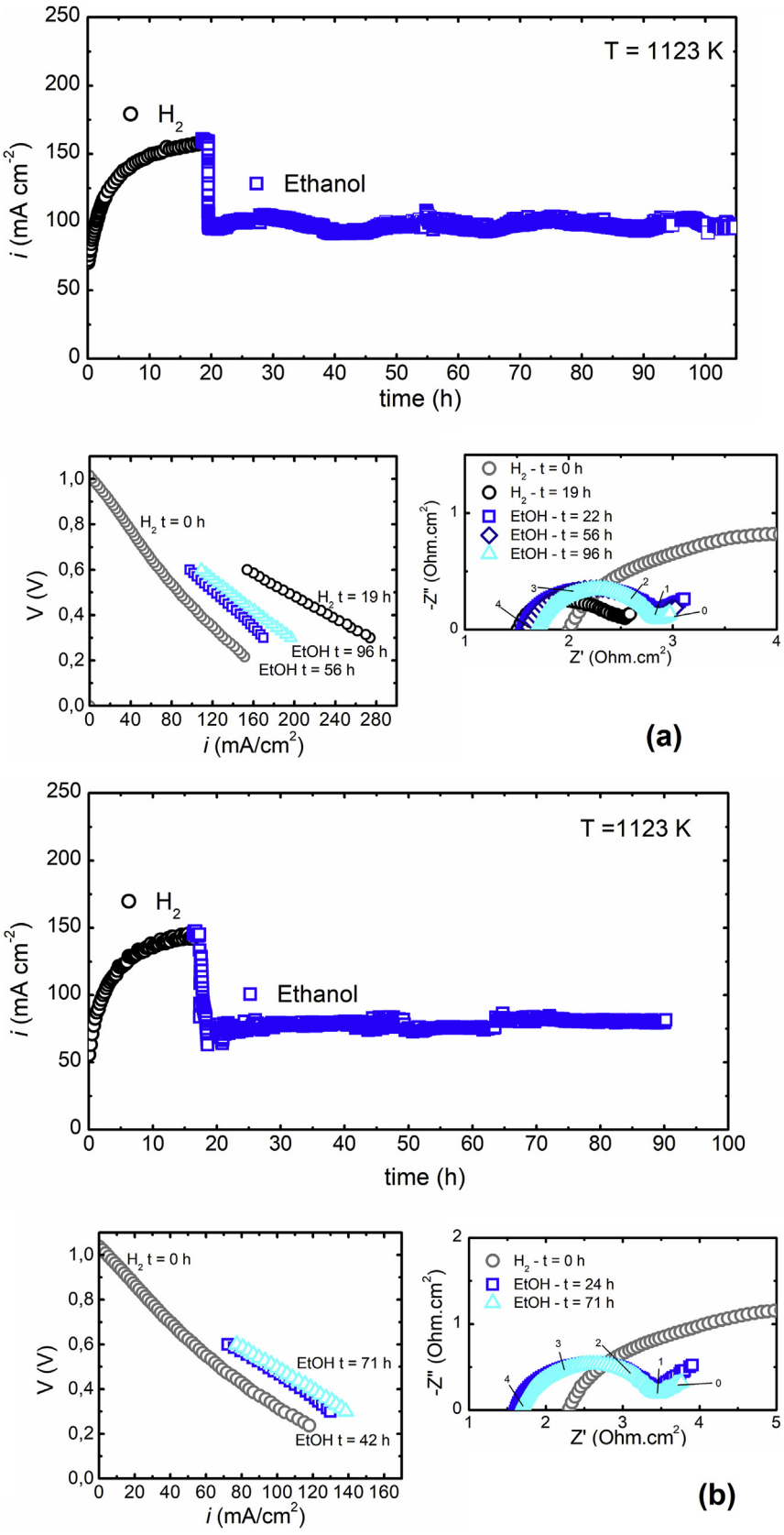

Fig. 10 – Durability tests at 1123 K and 0.6 V of fuel cells (CLFC) using (a) Ni/CeZr and (b) Ni/CeNb catalytic layer. The corresponding impedance diagrams and i x V curves measured at different times during the durability tests are shown on the bottom panel.

the theoretical number of electrons constant [13,98]. In previously reported studies using ceria-based catalytic layers (25 μm thickness) for direct ethanol SOFC, the current output for both H_2 and ethanol was comparable [13,14,98].This was an evidence that ethanol was steam-reformed in the catalytic layer and the produced hydrogen was electrochemically oxidized with good overall efficiency [14,98]. In the present study, possibly due to the microstructural features of the Ni/doped-ceria anode layers, changing H_2 to ethanol decreased the Faradaic efficiency of the fuel cell. Important parameters, such as porosity and anode layer thickness, must be optimized to attain high-performance fuel cells. Controlling the processing parameters to obtain similar microstructures of materials containing Zr and Nb was a hard task because of the different sintering characteristics (particle size distribution, agglomeration, etc), resulting from the different ceria dopants (Fig. 11). Nevertheless, our results provide an important comparison to evaluate the stability of the catalyst in direct (dry) ethanol SOFCs. In this context, the thickness of the anode layers was kept to a few microns (~10 μm) to evidence any possible deactivation of the catalyst due to carbon deposits. The fuel cell performance when H_2 was changed to ethanol was reflected on the impedance spectroscopy diagrams. As compared to H_2, impedance data taken under ethanol exhibit a slightly higher ohmic resistance and a more convoluted diagram, in which the polarization resistance increases and a spike at the low frequency end develops. The low frequency (spike) component is related to complex mass transport processes taking place in the fuel cell with internal reforming and requires further investigation [14,98]. The increase in both ohmic and polarization resistances agrees with the lower current output of the fuel cell under ethanol and can be ascribed to several factors related to the complex reactions taking place at the anode layers. The steam reforming reaction is strongly endothermic and can induce a local decrease of the temperature, ethanol and steam contribute to a higher p_{O2} as compared to H_2 that can promote a partial oxidation of Ni. Such effects can be associated with the increased impedance components measured under ethanol; however, further studies are underway to better clarify this point.

The main purpose of this study is to test Ni/CeZr and Ni/CeNb anode layers under the harshest conditions, in which ethanol is delivered directly to the fuel cell without any oxidant, such as water, to avoid carbon deposits. Thus, the most important experimental result is the stability of the fuel cells running on dry ethanol. Fuel cells were operated for approximately 100 h on dry ethanol without noticeable degradation due to carbon deposit accumulation. A closer inspection of the impedance diagrams measured during the stability tests show some interesting features (Figs. S12–S15 and Table S4). For both ESFC and CLFC, the ohmic resistance increased with increasing operating time. On the other hand, the polarization resistance exhibited a slight decrease with increasing measuring time. The impedance diagrams of CLFC samples showed that low and high frequency components of the polarization arc have distinct behaviors: the high frequency component increases, whereas the low frequency decreases with the operating time. Overall, the total resistance of the fuel cells on ethanol is not significantly changed during the long-term tests, in agreement with the stability observed in the *i vs.* time data. It is important to consider that carbon deposits were reported to build up rather fast (up to 4 h) in standard fuel cells running on (dry) hydrocarbons and ethanol [14]. Such quick deactivation is similar to the one observed in the ED reactions due to carbon formation and it is evident during the initial hours of fuel cell testing [14,99]. The stability of the Ni/doped-ceria cermets in fuel cell conditions was measured up to 100 h, greatly exceeding the typical time interval for observing fuel cell collapse due to carbon deposit formation.

The electrochemical characterization gives a strong indication that the studied Ni/doped-ceria cermets are efficient catalysts to avoid carbon formation in the operating conditions of direct ethanol SOFC. Such stability is achieved because the electrochemical oxidation of hydrogen produces water for ethanol steam reforming reaction [13,14]. Thus, under polarization at 0.6 V, the fuel cell resembles the conditions observed in the steam reforming reactions ESR shown in Fig. S5a–b. In agreement with ESR conditions, no deactivation due to carbon deposits was identified during fuel cell durability tests on (dry) ethanol. Ideally, the electrochemical oxidation of hydrogen produces an equimolar amount of water, whereas in the ESR 1 mol of ethanol consumes 3 mol of water to produce 6 mol of hydrogen (Eq. (7)). Therefore, provided that the fuel cell runs with a minimum fuel utilization (~30%), electrochemical combustion of hydrogen generates water in stoichiometric excess for the catalytic reaction producing hydrogen, and, thus, both reactions sustain each other [81]. This coupling of both electrochemical and catalytic reactions for internal reforming evidences the robustness of the Ni/doped-ceria cermet in such a harsh condition for the stability of the fuel cell.

As both fuel cell configurations (CLFC and ESFC) were very stable under ethanol, the main difference concerning the investigated ceria dopants was related to the electrical properties of the anode layers. As indicated by the electrochemical tests shown in Figs. 9 and 10, the main differences arise from the anode configuration. For the CLFCs, in which Ni/doped-ceria catalytic layer is not part of the electrical connection, the ohmic resistance of all specimens (~1.5 Ωcm^{-2}) corresponds to the ohmic resistance of the standard cell configuration using Ni/YSZ (60 wt% Ni) anode. In the CLFC configuration the Ni/doped-ceria cermet plays exclusively the role of the catalyst and no significant differences on the power output were observed between the samples with both Zr and Nb doping. This is an indication that Ni controls the catalytic properties for ethanol steam reforming as long the doped-ceria support contributes for the reaction stability by different mechanisms, as previously discussed for Zr and Nb dopants in section ED and SR of ethanol in a fixed-bed reactor. Such a feature is supported by the comparable values of the polarization resistance measured for all the CLFC samples (~1.5 Ωcm^{-2}), regardless of the compound used in the catalytic layer. On the other hand, for ESFC the Ni/doped-ceria is used as the anode (current collector layer) and the electrical properties of the doped-ceria support are expected to change the electrical properties of the fuel cell. The ohmic resistance values of the ESFC samples were higher than those of CLFC due to the lower volume fraction of Ni in the Ni/doped-ceria anode as compared to the standard Ni/YSZ anode (60 wt%

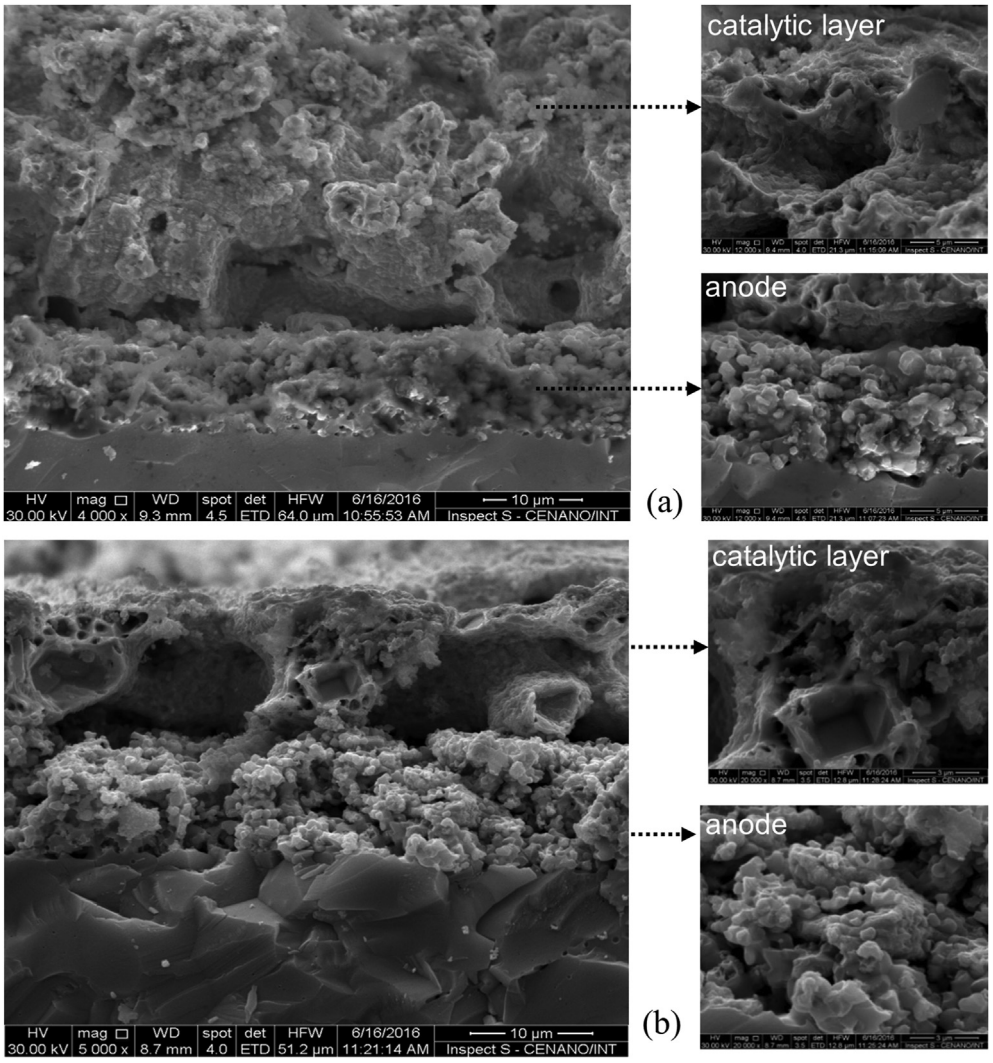

Fig. 11 – Post-test analyses of (a) Ni/CeNb and (b) Ni/CeZr as catalytic layer operating on dry ethanol at 1173 K: SEM images of the interface between anode support and catalytic layer.

Ni). The ceria-zirconia solid solution is known to exhibit good oxygen ion conductivity, whereas Nb-doped ceria has a strong electronic contribution. Such features were confirmed by the electrical conductivity measurements shown in Fig. 8. Notably, the ESFC with Ni/CeNb CCL exhibited lower current output due to higher ohmic and polarization resistances than the Ni/CeZr, as inferred from the impedance data. Such a higher resistance is in agreement with a resistive secondary phase formation observed in the CeNb support. Nevertheless, the ESFC samples, in which both the catalytic and electrochemical reactions took place in the same layer, were very stable towards ethanol. Thus, the experimental data indicate that, the ceria supports exhibit distinct electrical properties and oxygen storage capacities that result in different mechanisms for a stable ethanol SR reaction.

The absence of carbon deposits was further confirmed by SEM analyses after ethanol stability tests. The SEM image of the cross section of the CLFC samples are shown in Fig. 11. Detailed investigation by SEM revealed no indication of the formation of carbon filaments typically observed on the catalysts after ED tests previously discussed.

Taking into account the results of catalytic tests and of both SEM and TG analyses, it is likely that the internal SR of ethanol takes place in the Ni/doped-ceria cermets. Differently from the ED reaction, the water resulting from the electrochemical reactions promotes internal SR and inhibits carbon formation. Thus, the catalyst layer uses the steam produced by the electrochemical oxidation of hydrogen to react with ethanol to generate more hydrogen. Thus, both the electrochemical and the catalytic reactions sustain each other for the continuous operation of the fuel cell with dry ethanol [18].

Conclusions

Composites of NiO and doped-ceria using different ceria dopants were synthesized and characterized aiming at stable direct ethanol solid oxide fuel cells. The prepared composites, with Ni volume fraction above the percolation threshold for electronic transport, are active catalysts for ethanol steam reforming. Amongst the investigated dopants, Zr and Nb-doped ceria exhibited the smallest fraction

of carbon deposits, as inferred from post-reaction analyses after ethanol decomposition reaction in a fixed bed reactor. Such good catalytic properties arise from distinct mechanisms related to different properties of the ceria support depending on the dopant used. Both Zr and Nb-doped ceria have markedly different transport properties; while Zr-doped ceria is known for high oxygen storage capacity, doping ceria with 10 mol% of Nb results in increased electronic conductivity and the formation of an insulating second phase. Such electrical and microstructural features influenced the catalytic properties of the cermet because of the different interaction between the ceria support and Ni depending on the ceria dopant. In standard electrolyte supported fuel cells, the different electrical conductivities of the Ni-ceria cermets anode current collector layer resulted in different performance. However, the transport properties of the doped-ceria play no role when the cermet was used as an additional catalytic layer. Thus, fuel cells displayed similar performances using the Ni/ceria cermets as catalytic layer irrespectively of the ceria dopant. More importantly, in both configurations of fuel cell anodes studied the Ni-ceria cermets showed a very stable performance for 100 h of continuous operation under dry ethanol clearly indicating that catalytic steam reforming and hydrogen electrochemical oxidation reactions are sustaining each other. Such results evidenced that ceria-based cermets using Ni are effective anode materials for internal reforming in direct ethanol solid oxide fuel cells.

Declaration of competing interest

The authors declare that they have no known competing financial interests or personal relationships that could have appeared to influence the work reported in this paper.

Acknowledgements

Authors acknowledge the support of Brazilian agencies. AAAS is thankful for the CNPq and CAPES scholarships. FCF is thankful for the financial support of CNEN and the research funding by FAPESP grants 2013/26961-7, 2014/09087-4, 2014/50279-4, and 2017/11937-4. Authors are thankful to LNLS for granting time to use the beam at XPD (XPD-20150237) and for helping with diffraction studies. FCF, FBN, and LVM are CNPq fellow researchers.

Appendix A. Supplementary data

Supplementary data to this article can be found online at https://doi.org/10.1016/j.ijhydene.2020.10.155.

REFERENCES

[1] Brito J, Carbone S, Monteiro Dos Santos DA, Dominutti P, de Oliveira Alves N, Rizzo L, et al. Disentangling vehicular emission impact on urban air pollution using ethanol as a tracer. Sci Rep 2018;8:10679–89. https://doi.org/10.1038/s41598-018-29138-7.

[2] Dogdibegovic E, Fukuyama Y, Tucker MC. Ethanol internal reforming in solid oxide fuel cells: a path toward high performance metal-supported cells for vehicular applications. J Power Sources 2020;227598:449. https://doi.org/10.1016/j.jpowsour.2019.227598.

[3] Douvartzides SL, Coutelieris FA, Demin AK, Tsiakaras PE. Electricity from ethanol fed SOFCs: the expectations for sustainable development and technological benefits. Int J Hydrogen Energy 2004;29:375–9. https://doi.org/10.1016/S0360-3199(03)00047-8.

[4] Arpornwichanop A, Chalermpanchai N, Patcharavorachot Y, Assabumrungrat S, Tade M. Performance of an anode-supported solid oxide fuel cell with direct-internal reforming of ethanol. Int J Hydrogen Energy 2009;34:7780–8. https://doi.org/10.1016/j.ijhydene.2009.07.006.

[5] McIntosh S, Gorte RJ. Direct hydrocarbon solid oxide fuel cells. Chem Rev 2004;104:4845–65. https://doi.org/10.1021/cr020725g.

[6] Ni M, Leung DYC, Leung MKH. A review on reforming bio-ethanol for hydrogen production. Int J Hydrogen Energy 2007;32:3238–47. https://doi.org/10.1016/j.ijhydene.2007.04.038.

[7] Thanomjit C, Patcharavorachot Y, Ponpesh P, Arpornwichanop A. Thermodynamic analysis of solid oxide fuel cell system using different ethanol reforming processes. Int J Hydrogen Energy 2015;40:6950–8. https://doi.org/10.1016/j.ijhydene.2015.03.155.

[8] Atkinson A, Barnett S, Gorte RJ, Irvine JTS, McEvoy AJ, Mogensen M, et al. Advanced anodes for high-temperature fuel cells. Nat Mater 2004;3:17–27. https://doi.org/10.1038/nmat1040.

[9] Zhan Z, Barnett SA. Use of a catalyst layer for propane partial oxidation in solid oxide fuel cells. Solid State Ionics 2005;176:871–9. https://doi.org/10.1016/j.ssi.2004.12.005.

[10] Klein JM, Hnault M, Ǵlin P, Bultel Y, Georges S. A solid oxide fuel cell operating in gradual internal reforming conditions under pure dry methane. Electrochem Solid-State Letters 2008;11. https://doi.org/10.1149/1.2936228.

[11] Vernoux P. Gradual internal methane reforming in intermediate-temperature solid-oxide fuel cells. J Electrochem Soc 1998;3487:145. https://doi.org/10.1149/1.1838832.

[12] Chen Y, DeGlee B, Tang Y, Wang Z, Zhao B, Wei Y, et al. A robust fuel cell operated on nearly dry methane at 500 °C enabled by synergistic thermal catalysis and electrocatalysis. Nature Energy 2018;3:1042–50. https://doi.org/10.1038/s41560-018-0262-5.

[13] Nobrega SD, Gelin P, Georges S, Steil MC, Augusto BL, Noronha FB, et al. A fuel-flexible solid oxide fuel cell operating in gradual internal reforming. J Electrochem Soc 2014;161:F354–9. https://doi.org/10.1149/2.107403jes.

[14] Steil MC, Nobrega SD, Georges S, Gelin P, Uhlenbruck S, Fonseca FC. Durable direct ethanol anode-supported solid oxide fuel cell. Appl Energy 2017;199:180–6. https://doi.org/10.1016/j.apenergy.2017.04.086.

[15] Zhao J, Xu X, Li M, Zhou W, Liu S, Zhu Z. Coking-resistant Ce0.8Ni0.2O2-δ internal reforming layer for direct methane solid oxide fuel cells. Electrochim Acta 2018;282:402–8. https://doi.org/10.1016/j.electacta.2018.06.088.

[16] Huang B. Zhu X jian, Hu W qi, Wang Y yun, Yu Q chun. Characterization of the Ni-ScSZ anode with a LSCM-CeO2 catalyst layer in thin film solid oxide fuel cell running on ethanol fuel. J Power Sources 2010;195:3053–9. https://doi.org/10.1016/j.jpowsour.2009.11.126.

[17] Lo Faro M, Reis RM, Saglietti GGA, Oliveira VL, Zignani SC, Trocino S, et al. Solid oxide fuel cells fed with dry ethanol:

the effect of a perovskite protective anodic layer containing dispersed Ni-alloy @ FeOx core-shell nanoparticles. Applied Catalysis B: Environmental 2018;220:98–110. https://doi.org/10.1016/j.apcatb.2017.08.010.
[18] Augusto BL, Noronha FB, Fonseca FC, Tabuti FN, Colman RC, Mattos LV. Nickel/gadolinium-doped ceria anode for direct ethanol solid oxide fuel cell. Int J Hydrogen Energy 2014;39:11196–209. https://doi.org/10.1016/j.ijhydene.2014.05.088.
[19] Modafferi V, Panzera G, Baglio V, Frusteri F, Antonucci PL. Propane reforming on Ni-Ru/GDC catalyst: H2 production for IT-SOFCs under SR and ATR conditions. Appl Catal Gen 2008;334:1–9. https://doi.org/10.1016/j.apcata.2007.10.006.
[20] Jasinski P, Suzuki T, Petrovsky V, Anderson HU. Nanocomposite nickel ceria cermet with low nickel content for anode-supported SOFCs. Electrochem Solid State Lett 2005;8:6–9. https://doi.org/10.1149/1.1869153.
[21] Muccillo R, Muccillo ENS, Fonseca FC, de Florio DZ. Characteristics and performance of electrolyte-supported solid oxide fuel cells under ethanol and hydrogen. J Electrochem Soc 2008;155:B232. https://doi.org/10.1149/1.2828024.
[22] Zhi X, Gan T, Hou N, Fan L, Yao T, Wang J, et al. ZnO-promoted surface diffusion on NiO-Ce0.8Sm0.2O1.9 anode for solid oxide fuel cell. J Power Sources 2019;423:290–6. https://doi.org/10.1016/j.jpowsour.2019.03.088.
[23] Isarapakdeetham S, Kim-Lohsoontorn P, Wongsakulphasatch S, Kiatkittipong W, Laosiripojana N, Gong J, et al. Hydrogen production via chemical looping steam reforming of ethanol by Ni-based oxygen carriers supported on CeO2 and La2O3 promoted Al2O3. Int J Hydrogen Energy 2019;45:1477–91. https://doi.org/10.1016/j.ijhydene.2019.11.077.
[24] Hołówko B, Błaszczak P, Chlipała M, Gazda M, Wang SF, Jasiński P, et al. Structural and catalytic properties of ceria layers doped with transition metals for SOFCs fueled by biogas. Int J Hydrogen Energy 2020;45:12982–96. https://doi.org/10.1016/j.ijhydene.2020.02.144.
[25] Ideris A, Croiset E, Pritzker M, Amin A. Direct-methane solid oxide fuel cell (SOFC) with Ni-SDC anode-supported cell. Int J Hydrogen Energy 2017;42:23118–29. https://doi.org/10.1016/j.ijhydene.2017.07.117.
[26] Escudero MJ, Serrano JL. Individual impact of several impurities on the performance of direct internal reforming biogas solid oxide fuel cell using W-Ni-CeO2 as anode. Int J Hydrogen Energy 2019;44:20616–31. https://doi.org/10.1016/j.ijhydene.2019.06.028.
[27] González-Velasco JR, Entrena J, González-Marcos JA, Gutiérrez-Ortiz JI, Gutiérrez-Ortiz MA. Preparation, activity and durability of promoted platinum catalysts for automotive exhaust control. Applied Catalysis B. Environmental 1994;3:191–204. https://doi.org/10.1016/0926-3373(93)E0030-F.
[28] Whittington BI, Jiang CJ, Trimm DL. Vehicle exhaust catalysis: I. The relative importance of catalytic oxidation, steam reforming and water-gas shift reactions. Catal Today 1995;26:41–5. https://doi.org/10.1016/0920-5861(95)00093-U.
[29] González-Velasco JR, Botas JA, González-Marcos JA, Gutiérrez-Ortiz MA. Influence of water and hydrocarbon processed in feedstream on the three-way behaviour of platinum-alumina catalysts. Appl Catal B Environ 1997;12:61–79. https://doi.org/10.1016/S0926-3373(96)00058-6.
[30] Rao GR, Kašpar J, Meriani S, di Monte R, Graziani M. NO decomposition over partially reduced metallized CeO2-ZrO2 solid solutions. Catal Lett 1994;24:107–12. https://doi.org/10.1007/BF00807380.
[31] Kröger FA, Vink HJ. Relations between the concentrations of imperfections in crystalline solids. Solid State Phy - Adv Res Appl 1956;3:307–435. https://doi.org/10.1016/S0081-1947(08)60135-6.
[32] Baidya T, Hegde MS, Gopalakrishnan J. Oxygen-release/storage properties of Ce0.5M0.5O 2 (M = Zr, Hf) oxides: interplay of crystal chemistry and electronic structure. J Phys Chem B 2007;111:5149–54. https://doi.org/10.1021/jp070525e.
[33] Marina OA, Mogensen M. High-temperature conversion of methane on a composite gadolinia-doped ceria - gold electrode. Appl Catal Gen 1999;189:117–26. https://doi.org/10.1016/S0926-860X(99)00259-8.
[34] Sciazko A, Miyahara K, Komatsu Y, Shimura T, Jiao Z, Shikazono N. Influence of initial powder morphology on polarization characteristics of nickel/gadolinium-doped-ceria solid oxide fuel cells electrode. J Electrochem Soc 2019;166:F44–52. https://doi.org/10.1149/2.0181902jes.
[35] Yashima M, Arashi H, Kakihana M, Yoshimura M. Raman scattering study of cubic–tetragonal phase transition in Zr1−xCexO2 solid solution. J Am Ceram Soc 1994;77:1067–71. https://doi.org/10.1111/j.1151-2916.1994.tb07270.x.
[36] Fornasiero P, Balducci G, Di Monte R, Kašpar J, Sergo V, Gubitosa G, et al. Modification of the redox behaviour of CeO2 induced by structural doping with ZrO2. J Catal 1996;164:173–83. https://doi.org/10.1006/jcat.1996.0373.
[37] Balducci G, Islam MS, Kaspar J, Fornasiero P, Graziani M. Bulk reduction oxygen migration in the ceria-based oxides. Chem Mater 2000;12:677–81. https://doi.org/10.1021/cm991089e.
[38] Boaro M, Trovarelli A, Hwang JH, Mason TO. Electrical and oxygen storage/release properties of nanocrystalline ceria-zirconia solid solutions. Solid State Ionics 2002;147:85–95. https://doi.org/10.1016/S0167-2738(02)00004-8.
[39] Fornasiero P, Dimonte R, Rao GR, Kaspar J, Meriani S, Trovarelli A, et al. Rh-loaded CeO2-ZrO2 solid-solutions as highly efficient oxygen exchangers: dependence of the reduction behavior and the oxygen storage capacity on the structural-properties. J Catal 1995;151:168–77. https://doi.org/10.1006/jcat.1995.1019.
[40] Rao GR, Fornasiero P, Kašpar J, Meriani S, Di Monte R, Graziani M. No decomposition over partially reduced metallized CeO2 containing catalysts. In: Frennet A, editor. Bastin J-MBT-S in SS and C, organizadores. Catalysis and automotive pollution control III, 96. Elsevier; 1995. p. 631–43. https://doi.org/10.1016/S0167-2991(06)81463-1.
[41] Aneggi E, Boaro M, De Leitenburg C, Dolcetti G, Trovarelli A. Insights into the redox properties of ceria-based oxides and their implications in catalysis. J Alloys Compd 2006;408–412:1096–102. https://doi.org/10.1016/j.jallcom.2004.12.113.
[42] Kašpar J, Fornasiero P, Graziani M. Use of CeO2-based oxides in the three-way catalysis. Catal Today 1999;50:285–98. https://doi.org/10.1016/S0920-5861(98)00510-0.
[43] Ahn K, He H, Vohs JM, Gorte RJ. Enhanced thermal stability of SOFC anodes made with CeO2 -ZrO2 solutions. Electrochem Solid State Lett 2005;8:A414. https://doi.org/10.1149/1.1945374.
[44] Janvier C, Pijolat M, Valdivieso F, Soustelle M. In: Thermodynamic description of the nonstoichiometric defect structure in Ce1-xZrxO2 solid solution powders, 127; 2000. https://doi.org/10.1016/S0167-2738(99)00289-1.
[45] O'Connell M, Morris MA. New ceria-based catalysts for pollution abatement. Catal Today 2000;59:387–93. https://doi.org/10.1016/S0920-5861(00)00303-5.
[46] Zhao S, Gorte RJ. A comparison of ceria and Sm-doped ceria for hydrocarbon oxidation reactions. Applied Catalysis A: Gene (Amst) 2004;277:129–36. https://doi.org/10.1016/j.apcata.2004.09.003.

[47] Zhao S, Gorte RJ. The effect of oxide dopants in ceria on n-butane oxidation. Applied Catalysis A: Gene (Amst) 2003;248:9–18. https://doi.org/10.1016/S0926-860X(03)00102-9.
[48] McIntosh S, Vohs JM, Gorte RJ. An examination of lanthanide additives on the performance of Cu-YSZ cermet anodes. Electrochim Acta 2002;47:3815–21. https://doi.org/10.1016/S0013-4686(02)00352-3.
[49] Naik IK. Electrical conduction in Nb2O5-doped cerium dioxide. J Electrochem Soc 1979;562:126. https://doi.org/10.1149/1.2129086.
[50] Subbarao EC, Maiti HS. Solid electrolytes with oxygen ion conduction. Solid State Ionics 1984;11:317–38. https://doi.org/10.1016/0167-2738(84)90024-9.
[51] Ramírez-Cabrera E, Atkinson A, Chadwick D. Reactivity of ceria, Gd- and Nb-doped ceria to methane. Appl Catal B Environ 2002;36:193–206. https://doi.org/10.1016/S0926-3373(01)00299-5.
[52] Yashiro K, Suzuki T, Kaimai A, Matsumoto H, Nigara Y, Kawada T, et al. Electrical properties and defect structure of niobia-doped ceria. Solid State Ionics 2004;175:341–4. https://doi.org/10.1016/j.ssi.2004.01.066.
[53] Sahoo PP, Payne JL, Li M, Claridge JB, Rosseinsky MJ. Synthesis, structure and conductivity studies of co-doped ceria: CeO2-Sm2O3-Ta2O5 (Nb2O5) solid solution. J Phys Chem Solid 2015;76:82–7. https://doi.org/10.1016/j.jpcs.2014.07.019.
[54] Ramírez-Cabrera E, Laosiripojana N, Atkinson A, Chadwick D. In: Methane conversion over Nb-doped ceria. Catalysis Today, 78. Elsevier; 2003. p. 433–8. https://doi.org/10.1016/S0920-5861(02)00324-3.
[55] Cimenti M, Hill JM. Direct utilization of ethanol on ceria-based anodes for solid oxide fuel cells. Asia Pac J Chem Eng 2009;4:45–54. https://doi.org/10.1002/apj.182.
[56] Liao M, Wang W, Ran R, Shao Z. Development of a Ni-Ce0.8Zr0.2O2 catalyst for solid oxide fuel cells operating on ethanol through internal reforming. J Power Sources 2011;196:6177–85. https://doi.org/10.1016/j.jpowsour.2011.03.018.
[57] da Silva AAA, Bion N, Epron F, Baraka S, Fonseca FC, Rabelo-Neto RC, et al. Effect of the type of ceria dopant on the performance of Ni/CeO2 SOFC anode for ethanol internal reforming. Appl Catal B Environ 2017;206:626–41. https://doi.org/10.1016/j.apcatb.2017.01.069.
[58] Zimicz MG, Fábregas IO, Lamas DG, Larrondo SA. Effect of synthesis conditions on the nanopowder properties of Ce0.9Zr0.1O2. Mater Res Bull 2011;46:850–7. https://doi.org/10.1016/j.materresbull.2011.02.008.
[59] Kim P, Brett DJL, Brandon NP. The effect of water content on the electrochemical impedance response and microstructure of Ni-CGO anodes for solid oxide fuel cells. J Power Sources 2009;189:1060–5. https://doi.org/10.1016/j.jpowsour.2008.12.150.
[60] Kolodiazhnyi T, Sakurai H, Belik AA, Gornostaeva OV. Unusual lattice evolution and magnetochemistry of Nb doped CeO2. Acta Mater 2016;113:116–23. https://doi.org/10.1016/j.actamat.2016.04.052.
[61] Choudhury B, Choudhury A. Ce 3+ and oxygen vacancy mediated tuning of structural and optical properties of CeO 2 nanoparticles. Mater Chem Phys 2012;131:666–71. https://doi.org/10.1016/j.matchemphys.2011.10.032.
[62] Guo M, Lu J, Wu Y, Wang Y, Luo M. UV and visible Raman studies of oxygen vacancies in rare-earth-doped ceria. Langmuir 2011;27:3872–7. https://doi.org/10.1021/la200292f.
[63] Hong SJ, Virkar AV. Lattice parameters and densities of rare-earth oxide doped ceria electrolytes. J Am Ceram Soc 1995;78:433–9. https://doi.org/10.1111/j.1151-2916.1995.tb08820.x.
[64] Rey JFQ, Muccillo ENS. Lattice parameters of yttria-doped ceria solid electrolytes. J Eur Ceram Soc 2004;24:1287–90. https://doi.org/10.1016/S0955-2219(03)00498-9.
[65] Schmitt R, Nenning A, Kraynis O, Korobko R, Frenkel AI, Lubomirsky I, et al. A review of defect structure and chemistry in ceria and its solid solutions. Chem Soc Rev 2020;49:554–92. https://doi.org/10.1039/c9cs00588a.
[66] Lucid AK, Keating PRL, Allen JP, Watson GW. Structure and reducibility of CeO 2 doped with trivalent cations. https://doi.org/10.1021/acs.jpcc.6b08118; 2016.
[67] Bishop SR, Marrocchelli D, Fang W, Amezawa K, Yashiro K, Watson GW. Reducing the chemical expansion coefficient in ceria by addition of zirconia. Energy Environ Sci 2013;6:1142–6. https://doi.org/10.1039/c3ee23917a.
[68] Marrocchelli D, Bishop SR, Tuller HL, Yildiz B. Understanding chemical expansion in non-stoichiometric oxides: ceria and zirconia case studies. Adv Funct Mater 2012;22:1958–65. https://doi.org/10.1002/adfm.201102648.
[69] Keating PRL, Scanlon DO, Morgan BJ, Galea NM, Watson GW. Analysis of intrinsic defects in CeO 2 using a koopmans-like GGA+ U approach. J Phys Chem C 2012;116:2443–52. https://doi.org/10.1021/jp2080034.
[70] Thompson JG, Withers RL, Brink FJ. Modulated structures in oxidized cerium niobates. J Solid State Chem 1999;143:122–31. https://doi.org/10.1006/jssc.1998.8096.
[71] Dong WS, Roh HS, Jun KW, Park SE, Oh YS. Methane reforming over Ni/Ce-ZrO2 catalysts: effect of nickel content. Appl Catal Gen 2002;226:63–72. https://doi.org/10.1016/S0926-860X(01)00883-3.
[72] Augusto BL, Costa LOO, Noronha FB, Colman RC, Mattos LV. Ethanol reforming over Ni/CeGd catalysts with low Ni content. Int J Hydrogen Energy 2012;37:12258–70. https://doi.org/10.1016/j.ijhydene.2012.05.127.
[73] Fonseca Da RO, Da Silva AAA, Signorelli MRM, Rabelo-Neto RC, Noronha FB, Simões RCC, et al. Nickel/doped ceria solid oxide fuel cell anodes for dry reforming of methane. J Braz Chem Soc 2014;25:2356–63. https://doi.org/10.5935/0103-5053.20140245.
[74] Savova B, Loridant S, Filkova D, Millet JMM. Ni-Nb-O catalysts for ethane oxidative dehydrogenation. Appl Catal Gen 2010;390:148–57. https://doi.org/10.1016/j.apcata.2010.10.004.
[75] Heracleous E, Lemonidou AA. Ni-Nb-O mixed oxides as highly active and selective catalysts for ethene production via ethane oxidative dehydrogenation. Part II: mechanistic aspects and kinetic modeling. J Catal 2006;237:175–89. https://doi.org/10.1016/j.jcat.2005.11.003.
[76] Hu Z, Nakamura H, Kunimori K, Asano H, Uchijima T. Ethane hydrogenolysis and hydrogen chemisorption over niobia-promoted rhodium catalysts: a new phase by a strong rhodium-niobia interaction. J Catal 1988;112:478–88. https://doi.org/10.1016/0021-9517(88)90163-7.
[77] Hu Z, Nakamura H, Kunimori K, Yokoyama Y, Asano H, Soma M, et al. Structural transformation in Nb2O5-promoted Rh catalysts during calcination and reduction treatments. J Catal 1989;119:33–46. https://doi.org/10.1016/0021-9517(89)90132-2.
[78] Mattos LV, Jacobs G, Davis BH, Noronha FB. Production of hydrogen from ethanol: review of reaction mechanism and catalyst deactivation. Chem Rev 2012;112:4094–123. https://doi.org/10.1021/cr2000114.
[79] Zhan Z, Liu J, Barnett SA. Operation of anode-supported solid oxide fuel cells on propane-air fuel mixtures. Appl Catal Gen 2004;262:255–9. https://doi.org/10.1016/j.apcata.2003.11.033.
[80] De Lima SM, Da Silva AM, Da Costa LOO, Graham UM, Jacobs G, Davis BH, et al. Study of catalyst deactivation and reaction mechanism of steam reforming, partial oxidation,

and oxidative steam reforming of ethanol over Co/CeO 2 catalyst. J Catal 2009;268:268–81. https://doi.org/10.1016/j.jcat.2009.09.025.
[81] de Lima SM, da Cruz IO, Jacobs G, Davis BH, Mattos LV, Noronha FB. Steam reforming, partial oxidation, and oxidative steam reforming of ethanol over Pt/CeZrO2 catalyst. J Catal 2008;257:356–68. https://doi.org/10.1016/j.jcat.2008.05.017.
[82] de Lima SM, da Silva AM, da Costa LOO, Assaf JM, Jacobs G, Davis BH, et al. Evaluation of the performance of Ni/La2O3 catalyst prepared from LaNiO3 perovskite-type oxides for the production of hydrogen through steam reforming and oxidative steam reforming of ethanol. Appl Catal Gen 2010;377:181–90. https://doi.org/10.1016/j.apcata.2010.01.036.
[83] Moraes TS, Neto RCR, Ribeiro MC, Mattos LV, Kourtelesis M, Verykios X, et al. Effects of ceria morphology on catalytic performance of Ni/CeO2 catalysts for low temperature steam reforming of ethanol. Top Catal 2015;58:281–94. https://doi.org/10.1007/s11244-015-0369-x.
[84] Fatsikostas AN, Verykios XE. Reaction network of steam reforming of ethanol over Ni-based catalysts. J Catal 2004;225:439–52. https://doi.org/10.1016/j.jcat.2004.04.034.
[85] Galetti AE, Gomez MF, Arrúa LA, Abello MC. Hydrogen production by ethanol reforming over NiZnAl catalysts. Influence of Ce addition on carbon deposition. Appl Catal A: Gene (Amst) 2008;348:94–102. https://doi.org/10.1016/j.apcata.2008.06.039.
[86] Sánchez-Sánchez MC, Navarro RM, Fierro JLG. Ethanol steam reforming over Ni/Mx Oy-Al2 O3 (M = Ce, La, Zr and Mg) catalysts: influence of support on the hydrogen production. Int J Hydrogen Energy 2007;32:1462–71. https://doi.org/10.1016/j.ijhydene.2006.10.025.
[87] Natile MM, Poletto F, Galenda A, Glisenti A, Montini T, De Rogatis L, et al. La0.6Sr0.4Co1-yFeyO 3-δ perovskites: influence of the Co/Fe atomic ratio on properties and catalytic activity toward alcohol steam-reforming. Chem Mater 2008;20:2314–27. https://doi.org/10.1021/cm703329k.
[88] Song H, Ozkan US. Ethanol steam reforming over Co-based catalysts: role of oxygen mobility. J Catal 2009;261:66–74. https://doi.org/10.1016/j.jcat.2008.11.006.
[89] Pereira EB, Homs N, Martí S, Fierro JLG, Ramírez de la Piscina P. Oxidative steam-reforming of ethanol over Co/SiO2, Co-Rh/SiO2 and Co-Ru/SiO2 catalysts: catalytic behavior and deactivation/regeneration processes. J Catal 2008;257:206–14. https://doi.org/10.1016/j.jcat.2008.05.001.
[90] Rabelo-Neto RC, Sales HBE, Inocêncio CVM, Varga E, Oszko A, Erdohelyi A, et al. CO2 reforming of methane over supported LaNiO3 perovskite-type oxides. Appl Catal B Environ 2018;221:349–61. https://doi.org/10.1016/j.apcatb.2017.09.022.
[91] Haller GL, Resasco DE. Metal–support interaction: group VIII metals and reducible oxides. Adv Catal 1989;36:173–235. https://doi.org/10.1016/S0360-0564(08)60018-8.
[92] Da Silva ALM, Den Breejen JP, Mattos LV, Bitter JH, De Jong KP, Noronha FB. Cobalt particle size effects on catalytic performance for ethanol steam reforming - smaller is better. J Catal 2014;318:67–74. https://doi.org/10.1016/j.jcat.2014.07.020.
[93] Inaba H, Tagawa H. Ceria-based solid electrolytes. Solid State Ionics 1996;83:1–16. https://doi.org/10.1016/0167-2738(95)00229-4.
[94] De Guire MR, Shingler MJ, Dincer E. Point defect analysis and microstructural effects in pure and donor-doped ceria. Solid State Ionics 1992;52:155–63. https://doi.org/10.1016/0167-2738(92)90101-T.
[95] Lee JH, Yoon SM, Kim BK, Lee HW, Song HS. Electrical conductivity and defect structure of CeO2-ZrO2 mixed oxide. J Mater Sci 2002;37:1165–71. https://doi.org/10.1023/A:1014363304942.
[96] Fonseca FC, de Florio DZ, Esposito V, Traversa E, Muccillo ENS, Muccillo R. Mixed ionic–electronic YSZ/Ni composite for SOFC anodes with high electrical conductivity. J Electrochem Soc 2006;153:A354. https://doi.org/10.1149/1.2149312.
[97] Soman AK, Kuppusami P, Rabel AM. Electrical conductivity of NiO-gadolinia doped ceria anode material for intermediate temperature solid oxide fuel cells. Nano Hybrids and Composites 2017;17:224–36. https://doi.org/10.4028/www.scientific.net/nhc.17.224.
[98] Nobrega SD, Galesco MV, Girona K, De Florio DZ, Steil MC, Georges S, et al. Direct ethanol solid oxide fuel cell operating in gradual internal reforming. J Power Sources 2012;213:156–9. https://doi.org/10.1016/j.jpowsour.2012.03.104.
[99] Ferlauto AS, De Florio DZ, Fonseca FC, Esposito V, Muccillo R, Traversa E, et al. Chemical vapor deposition of multi-walled carbon nanotubes from nickel/yttria-stabilized zirconia catalysts. Appl Phys Mater Sci Process 2006;84:271–6. https://doi.org/10.1007/s00339-006-3617-x.